AGU PUBLICATIONS

JGR

Journal of Geophysical Research: Space Physics

RESEARCH ARTICLE

10.1002/2013JA019378

Heating of the sunlit polar cap ionosphere by reflected photoelectrons

R. H. Varney[1], S. C. Solomon[1], and M. J. Nicolls[2]

[1]High Altitude Observatory, National Center for Atmospheric Research, Boulder, Colorado, USA, [2]Center for Geospace Studies, SRI International, Menlo Park, California, USA

Key Points:
- Reflected photoelectrons are a significant source of heat for the polar cap
- Reflection potentials of tens of eV are needed to prevent cold electron inflow
- Simulations with reflected photoelectrons can reproduce RISR-N temperatures

Correspondence to:
R. H. Varney,
rvarney@ucar.edu

Citation:
Varney, R. H., S. C. Solomon, and M. J. Nicolls (2014), Heating of the sunlit polar cap ionosphere by reflected photoelectrons, *J. Geophys. Res. Space Physics*, *119*, 8660–8684, doi:10.1002/2013JA019378.

Received 27 AUG 2013
Accepted 27 SEP 2014
Accepted article online 1 OCT 2014
Published online 28 OCT 2014

Abstract Photoelectrons escape from the ionosphere on sunlit polar cap field lines. In order for those field lines to carry zero current without significant heavy ion outflow or cold electron inflow, field-aligned potential drops must form to reflect a portion of the escaping photoelectron population back to the ionosphere. Using a 1-D ionosphere-polar wind model and measurements from the Resolute Bay Incoherent Scatter Radar (RISR-N), this paper shows that these reflected photoelectrons are a significant source of heat for the sunlit polar cap ionosphere. The model includes a kinetic suprathermal electron transport solver, and it allows energy input from the upper boundary in three different ways: thermal conduction, soft precipitation, and potentials that reflect photoelectrons. The simulations confirm that reflection potentials of several tens of eV are required to prevent cold electron inflow and demonstrate that the flux tube integrated change in electron heating rate (FTICEHR) associated with reflected photoelectrons can reach 10^9 eV cm^{-2} s^{-1}. Soft precipitation can produce FTICEHR of comparable magnitudes, but this extra heating is divided among more electrons as a result of electron impact ionization. Simulations with no reflected photoelectrons and with downward field-aligned currents (FAC) primarily carried by the escaping photoelectrons have electron temperatures which are ~250–500 K lower than the RISR-N measurements in the 300–600 km region; however, simulations with reflected photoelectrons, zero FAC, and no other form of heat flux through the upper boundary can satisfactorily reproduce the RISR-N data.

1. Introduction

The polar wind is the extension of the topside ionosphere over the polar cap in which ions can outflow into the magnetosphere. The classical picture of the polar wind is as an ambipolar flow in which H^+ and He^+ escape the Earth's gravity at supersonic speeds but the heavier O^+ does not [*Axford*, 1968; *Banks and Holzer*, 1968, 1969a, 1969b]. The nonclassical polar wind includes other energization processes which can accelerate O^+ to escape energies and create nonthermal ion beams and conics (see *Yau and André* [1997], *André and Yau* [1997] *Moore et al.* [1999], and *Yau et al.* [2011] for reviews). Both the amount of light ions outflowing in the classical polar wind and the amount of heavy ions upflowing to regions where energization processes could be important are controlled by the plasma densities and temperatures in the *F* region and topside ionosphere [e.g., *Schunk*, 2007]. Thus, the energetics of the polar cap ionosphere is important to any study of the polar wind and ion outflow.

Knowledge of polar cap aeronomy has recently been greatly expanded by the deployment of the north face of the Resolute Bay Incoherent Scatter Radar (RISR-N) in 2009 [*Bahcivan et al.*, 2010]. At 82.77°N magnetic latitude, RISR-N is the highest magnetic latitude ISR ever constructed and the first ISR in the polar cap. RISR-N provides electron density, electron temperature, and ion temperature profiles in the 100–600 km region on a routine basis. The purpose of the present paper is to evaluate which physical processes are most important in determining the plasma temperatures in the 300–600 km region as measured by RISR-N. In the auroral zone and in the cusp the Poynting fluxes and particle precipitation fluxes from the magnetosphere dominate the ionospheric dynamics. For a polar cap station like Resolute Bay, however, the Joule heating and particle precipitation are expected to be small.

The polar ionosphere is heated both by the absorption of solar EUV and by inputs from the magnetosphere. In polar ionospheric models the downward electron heat flux from the upper boundary is a particularly difficult boundary condition to set. The simulations using the Polar Wind Outflow Model (PWOM) presented by *Glocer et al.* [2012] use values which map to -1.7×10^8 and -3.4×10^8 eV cm^{-2} s^{-1} at 6300 km. The mapping

is done by assuming the ratio of the heat flux to the magnetic field strength is constant along the field line and the magnetic field varies as r^{-3}, where r is the geocentric radius. During sunlit conditions small differences were observed between the simulations at these two values, but larger differences appeared at higher solar zenith angles. These heat fluxes are fairly small, however. In contrast, *Bekerat et al.* [2007] compared the ionospheric forecast model (IFM) to DMSP measurements of plasma density at 800 km and showed that without any heat flux the IFM systematically underestimated the measurements by a factor of 2 but that reasonable agreement could be achieved if heat fluxes of -5×10^9 to -1.5×10^{10} eV cm^{-2} s^{-1} were assumed at the top boundary of 1500 km. At 6300 km these values map to -1.2×10^9 to -3.6×10^9 eV cm^{-2} s^{-1}, which are an order of magnitude larger than the values used by *Glocer et al.* [2012]. The changes in the IFM daytime topside ionospheric profiles when such large heat fluxes are added are dramatic [*Bekerat et al.*, 2007].

Both of the aforementioned models (IFM and PWOM) add downward heat flux through the upper boundary as if it were transported by thermal conduction. The assumed heat flux is used with Fourier's law to set a boundary condition on the electron temperature gradient. In contrast, Akebono measurements of the thermal electron temperature anisotropy demonstrate that the electron heat flows in the polar wind point upward instead of downward [*Yau et al.*, 1995]. Energy can flow down into the ionosphere in many other forms, however. Electromagnetic energy fluxes (i.e., Poynting fluxes) will produce Joule heating, which primarily heats the ions and neutrals instead of the electrons. Energy flux carried by suprathermal electrons will both heat the thermal electrons through Coulomb collisions and excite and ionize neutrals through inelastic collisions. In the polar cap the suprathermal electrons propagating downward from the upper boundary can be divided into two classes: polar rain, i.e., soft precipitation of solar wind origin, and photoelectrons which are reflected by high-altitude potential structures.

Poleward of the region 1 current system the global configuration of the ionosphere-magnetosphere system dictates that the field-aligned currents (FACs) should be nearly zero. However, in the sunlit polar cap large fluxes of photoelectrons are able to escape from the ionosphere. Typical numbers for light ion outflow and polar rain are not large enough to balance the photoelectron escape fluxes [*Wilson et al.*, 1997]. Three options for achieving zero current remain. The first is an inflow of cold electrons from high altitudes; however, it is not known if a sufficient population of high-altitude cold electrons exists to supply this inflow. The second option is heavy ion outflow. Using kinetic simulations which include photoelectrons, *Tam et al.* [1995, 1998] have produced supersonic O^+ outflow. However, these simulations also predict electron temperatures well over 10^4 K, which are much higher than Akebono measurements [*Yau et al.*, 1995]. The third option is that high-altitude potential structures form which reflect many of the escaping photoelectron back into the ionosphere. *Wilson et al.* [1997] argued that this mechanism was the most reasonable, and in kinetic simulations *Wilson et al.* [1997] and *Su et al.* [1998] were able to find zero current solutions without cold electron inflow or heavy ion outflow by inserting double layers with potential drops of tens of eV. One possible formation mechanism for these double layers is a contact discontinuity which forms between the cold ionospheric electron gas and the hot magnetosheath electron gas [*Barakat and Schunk*, 1984; *Barakat et al.*, 1998b]. The simulations of *Barakat et al.* [1998b] show that these double layers form between 2 and 6 R_E in altitude, and their locations are highly dynamic as the field lines convect through different regions. In the sunlit polar cap the FAST spacecraft frequently observes downward moving photoelectrons which are a copy of the upward moving photoelectron distribution up to a cutoff energy and then nonexistent above that cutoff energy [*Kitamura et al.*, 2012]. These measurements prove that polar cap field lines usually, although not always, achieve zero current by creating high-altitude potential structures that reflect photoelectrons.

The history of polar wind modeling is extensive (for reviews, see *Ganguli* [1996], *Lemaire et al.* [2007], *Schunk* [2007] and *Tam et al.* [2007]). The model in the present paper was developed as a tool for examining different kinds of energy flows into the polar ionosphere but certainly does not capture all of the relevant physics. Section 2 describes this newly developed ionosphere-polar wind model which includes three different kinds of energy fluxes through the upper boundary: thermal conduction, soft precipitation (polar rain), and reflected photoelectrons. Section 3 shows example model runs with an emphasis on how different kinds of energy flows produce different profiles. Then section 4 compares model runs to RISR-N data. Finally, section 5 discusses the ramifications of the examples presented, and section 6 states the conclusions.

2. Model Description

The 1-D model used in this study couples a fluid description of ions and thermal electrons with a kinetic description of suprathermal electrons on a single vertical magnetic field line between 97 and 6300 km altitudes. Strictly speaking, the assumptions underlying fluid descriptions of the ions are only valid below the ion exobase, which is defined as the point where the ion mean free path equals the ion scale height and typically varies between 1500 and 3000 km altitudes [*Lemaire et al.*, 2007]. All of the data-model comparisons presented in this paper consider altitudes below 700 km where fluid theories are completely appropriate. The upper portion of the model serves as a computational buffer between the upper boundary and the region of interest. Tests have shown that the model results vary by only a few percent as the top boundary is moved between 3000 km and 8500 km. If the upper boundary were lower than 3000 km then the light ions would not necessarily be supersonic at the upper boundary. In this case the characteristic velocities are not all upward, and simple outflow upper boundary conditions cannot be used. In models with upper boundaries below the transition point, either the light ion outflow fluxes, upflow velocities, or Mach numbers need to be specified a priori.

The present study ignores ionospheric electrodynamics and thermospheric dynamics. The simulated field line is fixed in geographic latitude and longitude, the neutral densities and temperatures are taken from the NRLMSISE-00 empirical model [*Picone et al.*, 2002], and the vertical winds are set to zero. The magnetic field is assumed to be vertically oriented and vary with geocentric radius, r, as r^{-3}. These are both good approximations in the polar cap. The field-aligned ion dynamics are only influenced by the parallel (i.e., vertical) component of the neutral winds, and thus, the horizontal winds do not need to be specified. The neglect of convection is a serious limitation of the present model. The examples presented in this paper focus on times near the summer solstice when the convecting field lines are constantly sunlit.

Fluid theories are constructed by assuming the distribution functions have a particular form which is characterized by a small number of moments and then deriving equations for the evolution of these moments [e.g., *Schunk*, 1977]. *Blelly and Schunk* [1993] compared the four most commonly used fluid approximations in ionospheric physics for vertical open field lines. The systems of equations compared were the "standard set," which are the five-moment equations plus heat flows given by Fourier's law, the eight-moment equations, the thirteen-moment equations, and the sixteen-moment equations. It should be noted that the twenty-moment equations reduce to the sixteen-moment equations in the gyro-dominated limit [*Gombosi and Rasmussen*, 1991]. In the *F* region, *Blelly and Schunk* [1993] showed significant differences in the equilibrium electron densities and temperatures between the "standard set" and the eight-moment equations which they attributed to thermal diffusion, diffusion thermal, and thermoelectric effects which are absent from the "standard set" but included in the eight-moment, thirteen-moment, and sixteen-moment equations. The differences between the results of the eight-moment, thirteen-moment, and sixteen-moment simulations were less dramatic, especially in the densities and velocities. The eight-moment equations ignore temperature anisotropy, but temperature anisotropy should develop in the high-altitude region where the light ions are supersonic. Nonetheless, this temperature anisotropy has a relatively small influence on the resulting density and velocity profiles because in the supersonic region the ion dynamic pressure is larger than the ion thermal pressure. The inefficient communication between the higher and lower moments in the supersonic region explains why *Blelly and Schunk* [1993] observed relatively small changes in the density and velocity profiles between the eight-, thirteen-, and sixteen-moment equations. No fluid theory is rigorously justified in the collisionless polar wind [*Lemaire et al.*, 2007]; however, the present paper is focused on reflected photoelectrons which propagate down to the *F* region ionosphere. Photoelectron propagation is primarily influenced by the neutral and thermal electron density profiles, and thus, the eight-moment formulation is good enough for the narrow focus of the present study.

2.1. Eight-Moment Ion Equations

The eight-moment equations can be written in many different equivalent forms. One particularly elegant form results in conservation laws with additional nonconservative terms involving the ambipolar electric field. The variables in this form are the density, momentum density vector, energy density, and energy flow vector. The problem with this form is the heat flow vector is typically a small part of the total energy flow vector, which can lead to loss of precision problems. *Kőrösmezey et al.* [1993] discuss an analogous problem with the sixteen-moment equations. The model adopts a form of the eight-moment equations

which uses a heat flow equation instead of an energy flow equation but is otherwise stated in terms of conservative variables:

$$\frac{\partial}{\partial t}\left(An_i\right)+\frac{\partial}{\partial s}\left[An_iu_i\right]=A\frac{\delta n_i}{\delta t} \tag{1}$$

$$\frac{\partial}{\partial t}\left(An_iu_i\right)+\frac{\partial}{\partial s}\left[An_iu_i^2+A\frac{p_i}{m_i}\right]=\frac{A}{m_i}n_i\left(eE_\parallel-m_ig\right)+\frac{A}{m_i}p_i\frac{\partial \ln A}{\partial s}+\frac{A}{m_i}\frac{\delta M_i}{\delta t}+Au_i\frac{\delta n_i}{\delta t} \tag{2}$$

$$\frac{\partial}{\partial t}\left(\frac{A}{m_i}\epsilon_i\right)+\frac{\partial}{\partial s}\left[\frac{A}{m_i}\left(u_i\epsilon_i+u_ip_i+q_i\right)\right]=\frac{A}{m_i}n_iu_i\left(eE_\parallel-m_ig\right)+\frac{A}{m_i}\frac{\delta E_i'}{\delta t}+\frac{A}{m_i}u_i\frac{\delta M_i}{\delta t}+\frac{A}{m_i}\frac{\epsilon_i}{n_i}\frac{\delta n_i}{\delta t} \tag{3}$$

$$\frac{\partial}{\partial t}\left(\frac{A}{m_i}q_i\right)+\frac{\partial}{\partial s}\left[\frac{16}{5}\frac{A}{m_i}u_iq_i\right]=\frac{11}{5}u_i\frac{\partial}{\partial s}\left(\frac{A}{m_i}q_i\right)-\frac{5}{3}v_{Ti}^2\frac{\partial}{\partial s}\left(\frac{A}{m_i}\epsilon_i\right)+\frac{5}{3}v_{Ti}^2u_i\frac{\partial}{\partial s}\left(An_iu_i\right)+\left(\frac{5}{2}v_{Ti}^4-\frac{5}{6}v_{Ti}^2u_i^2\right)\frac{\partial}{\partial s}\left(An_i\right)-\frac{2}{5}\frac{A}{m_i}u_iq_i\frac{\partial \ln A}{\partial s}+\frac{A}{m_i}\frac{\delta q_i'}{\delta t}. \tag{4}$$

In the above equations m_i, n_i, u_i, p_i, and q_i are the ion mass, number density, field-aligned velocity, pressure, and field-aligned heat flow, respectively. The energy density is defined as $\epsilon_i = \frac{1}{2}m_in_iu_i^2+\frac{3}{2}p_i$, and the ion thermal speed is defined as $v_{Ti}=\sqrt{\frac{p_i}{n_im_i}}$. The spatial coordinate s increases with increasing altitude along the magnetic field line, $A \propto r^3$ is the cross-sectional area of the magnetic flux tube, g and $E_\parallel$ are the gravitational and parallel electric field strengths, and e is the elementary charge. The operator $\frac{\delta}{\delta t}$ denotes collisional terms.

Closed form expressions for all of the collisional terms needed in the five-moment equations which are valid for arbitrarily large temperature and velocity differences between species have been derived, but unfortunately, the same is not true for the eight-moment equations [*Schunk and Nagy*, 2009]. The Burgers linear collision terms are valid for small temperature and velocity differences, and the Burgers semilinear collision terms are valid for small velocity differences but arbitrary temperatures differences [*Burgers*, 1969; *Schunk and Nagy*, 2009]. In the polar wind the velocity differences between the light and heavy ions can exceed the ion thermal speeds, meaning the Burgers linear collision terms are not valid. The collision terms adopted for this study are the Burgers linear terms augmented with a few important terms from the general five-moment expressions:

$$\frac{\delta M_i}{\delta t}=-\sum_{j\neq i}n_im_i\nu_{ij}\left(u_i-u_j\right)\phi_{ij}-\sum_n n_im_i\nu_{in}\left(u_i-u_n\right)+\sum_{j\neq i}\frac{3}{5}\nu_{ij}\frac{\mu_{ij}}{k_BT_{ij}}\left(q_i-\frac{n_im_i}{n_jm_j}q_j\right)-\sum_r\frac{1}{5}\nu_{ir}\frac{\mu_{ir}}{k_BT_{ir}}\left(q_i-\frac{n_im_i}{n_rm_r}q_r\right) \tag{5}$$

$$\frac{\delta E_i'}{\delta t}=3n_i\nu_{ie}k_B\left(T_e-T_i\right)+\sum_{j\neq i}\frac{n_im_i}{m_i+m_j}\nu_{ij}\left[3k_B\left(T_j-T_i\right)\psi_{ij}+m_j\left(u_i-u_j\right)^2\phi_{ij}\right]+\sum_n\frac{n_im_i}{m_i+m_n}\nu_{in}\left[3k_B\left(T_n-T_i\right)+m_n\left(u_i-u_n\right)^2\right] \tag{6}$$

$$\frac{\delta q_i'}{\delta t}=-\frac{4}{5}\nu_{ii}q_i-\sum_{j\neq i}\nu_{ij}\left[q_i\left(D_{ij}^{(1)}+\frac{3}{2}\frac{\mu_{ij}T_i}{m_iT_{ij}}\right)-\frac{n_im_i}{n_jm_j}q_j\left(D_{ij}^{(4)}+\frac{3}{2}\frac{\mu_{ij}T_i}{m_iT_{ij}}\right)\right]-\sum_m\nu_{im}\left[q_iD_{im}^{(1)}-\frac{n_im_i}{n_mm_m}q_mD_{im}^{(4)}\right]-\sum_r\nu_{ir}\left[q_i\left(D_{ir}^{(1)}-\frac{1}{2}\frac{\mu_{ir}T_i}{m_iT_{ir}}\right)-\frac{n_im_i}{n_rm_r}q_r\left(D_{ir}^{(4)}-\frac{1}{2}\frac{\mu_{ir}T_i}{m_iT_{ir}}\right)\right]+\sum_{j\neq i}\nu_{ij}\frac{3}{2}p_i\frac{m_j}{m_i+m_j}\left(u_i-u_j\right)-\sum_r\nu_{ir}\frac{1}{2}p_i\frac{m_r}{m_i+m_r}\left(u_i-u_r\right). \tag{7}$$

In the above equations k_B is Boltzmann's constant, the $\nu_{\alpha\beta}$ are momentum transfer collision frequencies, and the reduced masses and temperatures are defined as [*Schunk and Nagy*, 2009]

$$\mu_{\alpha\beta} \equiv \frac{m_\alpha m_\beta}{m_\alpha + m_\beta} \tag{8}$$

$$T_{\alpha\beta} \equiv \frac{m_\alpha T_\beta + m_\beta T_\alpha}{m_\alpha + m_\beta}. \tag{9}$$

Note that $\frac{\delta E_i'}{\delta t}$ is related to the energy collision term defined by *Schunk and Nagy* [2009] by $\frac{\delta E_i'}{\delta t} \equiv \frac{\delta E_i}{\delta t} - \frac{3}{2} k_B T_i \frac{\delta n_i}{\delta t}$ and that (6) ignores any heating from chemical reactions.

In the collision term equations, summations over *j* refer to other ion species, summations over *r* refer to neutral species involved in resonant charge exchange with ion species *i*, summations over *m* refer to neutral species which cannot be involved in resonant charge exchange with ion species *i*, and sums over *n* refer to all neutral species. These equations were derived assuming ion-ion interactions are Coulomb collisions, nonresonant ion-neutral interactions are Maxwell molecule collisions, and resonant ion-neutral interactions are hard sphere interactions with a ratio of the Chapman-Cowling integrals, $\Omega^{(2,2)}/\Omega^{(1,1)}$, of 1 instead of the ordinary hard sphere value of 2 [cf. *Schunk*, 1975]. Expressions for the pure numbers $D_{ij}^{(1)}$, $D_{ij}^{(4)}$, $D_{im}^{(1)}$, and $D_{im}^{(4)}$ for Coulomb and Maxwell molecule collisions are given by *Schunk* [1977] and *Schunk and Nagy* [2009]. For the hard sphere-like treatment of resonant ion-neutral interactions, the corresponding numbers are

$$D_{ir}^{(1)} = \frac{3m_i^2 + \frac{13}{10} m_i m_r + \frac{9}{5} m_r^2}{\left(m_i + m_r\right)^2} \tag{10}$$

$$D_{ir}^{(4)} = \frac{4m_r^2 + \frac{1}{2} m_i m_r}{\left(m_i + m_r\right)^2}. \tag{11}$$

If the velocity correction terms ϕ_{ij} and ψ_{ij} were both set to unity, then (5)–(7) would be the Burgers linear collision terms. Instead, the model uses the expressions for these correction terms which come from the general five-moment collision terms for Coulomb collisions [see *Schunk*, 1977; *Schunk and Nagy*, 2009]. If the relative drift between ions *i* and *j* is small, these terms are both nearly unity, but if the relative drift becomes large compared to $\sqrt{\frac{2k_B T_{ij}}{\mu_{ij}}}$, these terms go to zero. When these terms are included Coulomb collisions become much less effective at driving the temperatures and velocities of the light and heavy ions toward each other in the polar wind.

Lastly, the chemical term $\frac{\delta n_i}{\delta t}$ is written as $P_i - L_i' n_i$, where P_i is a production rate and L_i' is a loss frequency. The production is the sum of photoproduction, production by suprathermal electron impact ionization, and chemical production. The chemical production and loss rates are computed using the reactions from the recent review of *Richards* [2011] plus the extra reactions listed in Appendix A. The photoproduction rates are computed from the high-resolution empirical solar EUV spectrum HEUVAC [*Richards et al.*, 2006] as described by *Varney* [2012]. The computation of the impact ionization rates from the suprathermal electron fluxes is described in detail by *Varney* [2012].

Many ions produced in the ionosphere have such short chemical lifetimes that transport can be ignored. In this model the eight-moment ion equations are only solved for H^+, He^+, and $O^+\left(^4S\right)$. The ions N^+, N_2^+, O_2^+, NO^+, $O^+\left(^2D\right)$, and $O^+\left(^2P\right)$ are assumed to have zero velocity, zero heat flow, temperatures equal to that of $O^+\left(^4S\right)$, and densities which evolve according (1) with the flux term neglected. Strictly speaking, transport of N^+ is not negligible above 300 km [*Richards*, 2011], but it is always such a small fraction of the total ion density that its dynamics are unimportant. The excited ion $O^+\left(^4P^*\right)$ is assumed to instantly decay to $O^+\left(^4S\right)$, and $O^+\left(^2P^*\right)$ is assumed to instantly decay to either $O^+\left(^2D\right)$ or $O^+\left(^2P\right)$ with equal probabilities [*Richards*, 2011].

2.2. Suprathermal Electron Equations

The model assumes the total electron distribution function is the sum of a thermal distribution and a suprathermal distribution. The thermal distribution is nearly Maxwellian and can be described by eight-moment transport equations, while the suprathermal distribution must be described using kinetic theory. At lower altitudes where collisions are important, the suprathermal electron density is assumed to

be small compared to the thermal electron density. This assumption allows the nonlinear terms describing collisions between suprathermal electrons to be neglected compared to the suprathermal-thermal electron collision terms. In this limit the suprathermal electron transport equation reduces to a linear equation which has a similar form to a radiative transfer equation [*Khazanov et al.*, 1994; *Schunk and Nagy*, 2009; *Varney*, 2012].

The form of the suprathermal electron transport equation used in this study is

$$\mu\frac{\partial}{\partial s}(A\Phi) - eE_{\parallel}\mu\frac{\partial}{\partial\mathcal{E}}(A\Phi) - \left(\frac{eE_{\parallel}}{\mathcal{E}} - \frac{\partial \ln A}{\partial s}\right)\frac{\partial}{\partial\mu}\left(\frac{1-\mu^2}{2}A\Phi\right) = AQ + A\frac{\delta\Phi}{\delta s}, \tag{12}$$

where $\mathcal{E}$ and μ are the kinetic energy and pitch angle cosine of the electrons, respectively, and Φ is the suprathermal electron flux [cf. *Khazanov et al.*, 1994]. The production function Q is the sum of photoproduction, cascade production, production from electron impact ionization, and production from quenching of $N(^2D)$ [*Varney et al.*, 2012]. The collision term is

$$\frac{\delta\Phi}{\delta s} = \frac{\partial}{\partial\mathcal{E}}\left[L(\mathcal{E})\Phi\right] + D(\mathcal{E})\frac{\partial}{\partial\mu}\left[\left(1-\mu^2\right)\frac{\partial\Phi}{\partial\mu}\right] - \sum_n\left(\bar{\sigma}_{an} + \bar{\sigma}_{en}\right)n_n\Phi + \sum_n\bar{\sigma}_{en}n_n\frac{1}{2}\int_{-1}^{1}\mathrm{d}\mu' p_{en}(\mathcal{E},\mu,\mu')\Phi(s,\mathcal{E},\mu'). \tag{13}$$

Expressions for the energy loss rate due to Coulomb collisions, $L(\mathcal{E})$, the pitch angle diffusion rate due to Coulomb collisions, $D(\mathcal{E})$, the total inelastic cross sections, $\bar{\sigma}_{an}$, and the total elastic cross sections, $\bar{\sigma}_{en}$, are given by *Varney et al.* [2012] and *Varney* [2012]. The work of *Varney et al.* [2012] assumed elastic collisions were isotropic; this study relaxes that assumption and uses the anisotropic phase functions, $p_{en}(\mathcal{E},\mu,\mu')$, from *Prasad et al.* [1985]. Degraded primaries from inelastic collisions, secondary electrons produced from impact ionization, and newly produced photoelectrons are all produced isotropically. The transport equation is solved using 16 pitch angle bins and a 107 bin nonuniformly spaced energy grid which extends up to 1 keV.

If the work done by parallel electric fields is ignored, suprathermal electrons will only move downward in energy and (13) can be solved one energy at a time starting at the highest energy bin in the grid [*Varney*, 2012]. One strategy for including the electric fields is to solve for all positions, pitch angles, and energies at once in a single large-sparse linear system solver [e.g., *Mantas*, 1975]. Another option is to rewrite the equation in terms of electron total energy (i.e., kinetic plus electrostatic potential) and then solve the equation one energy bin at a time on the total energy grid [*Liemohn et al.*, 1997]. This second approach is clearly the most elegant in the collisionless regime, but it greatly complicates the treatment of inelastic collisions. The approach used in this study is an iterative approach which is similar to the one developed by *Gustavsson and Eliasson* [2008] to model electron acceleration by an HF heater. The transport equation is solved one energy at a time using upwinded differences in energy space which depend on the sign of $\mu E_{\parallel}$ to approximate the $\frac{\partial}{\partial\mathcal{E}}$ term. Whenever these differences require a reference to the flux at the energy below the current energy, the flux from the previous iteration is used instead. The iteration continues until the RMS change in the computed heating rate between subsequent iterations is less than 10^{-4}, which typically only takes between 2 and 15 iterations.

2.3. Thermal Electron Equations

The thermal electron population could be described with a system of eight-moment equations similar to those used for the ions; however, the electron equations can be significantly simplified in the limit of small electron mass. On time scales much longer than the inverse electron plasma frequency the thermal electron density and flux can be determined from the quasineutrality and current continuity conditions:

$$n_e = \sum_i n_i - n_s \tag{14}$$

$$n_e u_e = \sum_i n_i u_i - \Gamma_s - \frac{A_{UB}}{A}\frac{J_{UB}}{e}, \tag{15}$$

where the *e* and *s* subscripts refer to thermal and suprathermal electron moments, respectively, the sums over *i* refer to sums over all ion species, and the needed moments of the suprathermal electron distribution are

$$n_s \equiv 2\pi \int_0^\infty \mathrm{d}\mathcal{E} \int_{-1}^{1} \mathrm{d}\mu \sqrt{\frac{m_e}{2\mathcal{E}}} \Phi \tag{16}$$

$$\Gamma_s \equiv 2\pi \int_0^\infty \mathrm{d}\mathcal{E} \int_{-1}^{1} \mathrm{d}\mu \, \mu \Phi. \tag{17}$$

These moments include all of the types of suprathermal electrons considered, including polar rain and reflected photoelectrons. The FAC density at the upper boundary, J_{UB}, is taken as an input, and A_{UB} is the field line cross-sectional area at the upper boundary.

In the limit of small electron mass the thermal electron heat flow equation reduces to the a steady state solution of [*Schunk and Nagy*, 2009]

$$q_e = -\kappa_e \frac{\partial T_e}{\partial s} + \frac{5}{2} \tilde{u}_e p_e, \tag{18}$$

where κ_e is the thermal conductivity, and the effective velocity in the thermoelectric term is

$$\tilde{u}_e \equiv \frac{3}{4} \sum_i \frac{\nu_{ei}}{\nu_{ec}} \left(u_e - u_i\right) + \frac{5}{4} \sum_n \frac{\nu_{en}}{\nu_{ec}} z_{en} \left(u_e - u_n\right) \tag{19}$$

$$\nu_{ec} \equiv \nu_{ee} + \frac{13}{8} \sum_i \nu_{ei} + \frac{5}{4} \nu_{en} z'_{en} \quad z_{en} \equiv 1 - \frac{2}{5} \frac{\Omega_{en}^{(1,2)}}{\Omega_{en}^{(1,1)}} \quad z'_{en} \equiv \frac{5}{2} + \frac{2}{5} \frac{\Omega_{en}^{(1,3)} - \Omega_{en}^{(1,2)}}{\Omega_{en}^{(1,1)}}$$

Expressions for the electron-electron collision frequency, ν_{ee}, the electron-ion collision frequencies, ν_{ei}, the electron-neutral collision frequencies, ν_{en}, and the Chapman-Cowling integrals for electron-neutral collisions, $\Omega_{en}^{(\ell,j)}$, are all taken from *Schunk and Nagy* [2009]. Compared to the transport coefficients computed by *Spitzer and Härm* [1953] using kinetic theory, the eight-moment value for the thermoelectric coefficient is very good, but the eight-moment value for the electron thermal conductivity is too small by more than a factor of 2 [*Schunk*, 1975]. Thus, while the model uses the eight-moment result for the thermoelectric term, it uses the widely used *Banks* [1966] expression for the electron thermal conductivity instead. This expression is identical to that used in Sami2 is another model of the ionosphere (SAMI2) [*Huba et al.*, 2000a].

The electrons obey an energy equation which has the same form as (3). Substituting (18) into that electron energy equation and taking the limit of small electron mass results in a simplified electron energy equation

$$\frac{\partial}{\partial t}\left(\frac{3}{2} A p_e\right) + \frac{\partial}{\partial s}\left[\frac{5}{2} A \left(u_e + \tilde{u}_e\right) p_e\right] = -A n_e u_e e E_\parallel + \frac{\partial}{\partial s}\left[A \kappa_e \frac{\partial T_e}{\partial s}\right] + A \frac{\delta E'_e}{\delta t} + A \frac{3}{2} k_B T_e \frac{\delta n_e}{\delta t}. \tag{20}$$

The term $\frac{\delta n_e}{\delta t}$ could be computed by insisting that all collisions and chemical reactions conserve charge, but ultimately this term is not directly computed by the model. The collisional heating and cooling term can be written in the form

$$\frac{\delta E'_e}{\delta t} = Q_{phe} - \sum_i n_e \nu_{ei} 3 k_B \left(T_e - T_i\right) - \sum_n L'_{en} \left(T_e - T_n\right). \tag{21}$$

The computation of the suprathermal electron heating rate, Q_{phe}, from the suprathermal flux is described by *Hoegy* [1984], *Varney et al.* [2012], and *Varney* [2012]. The heating rate is computed by summing all the energy lost by suprathermal electrons to Coulomb collisions, and the algorithm is guaranteed to numerically conserve energy [*Varney*, 2012]. Empirical expressions for the electron cooling rates due to inelastic collisions with neutrals, L_{en}, are given by *Schunk and Nagy* [2009]. The inelastic collisions considered excite N_2 rotation and vibration, O_2 rotation and vibration, O fine structure, and O $\left(^1\mathrm{D}\right)$. The term L'_{en} is defined as $L'_{en} \equiv L_{en}/(T_e - T_n)$, and this term is finite in the limit as $T_e \to T_n$ for all the inelastic processes considered.

2.4. Self-Consistent Electric Field

Appendix B derives the following expression for the ambipolar electric field:

$$E_{\parallel} = -\frac{1}{en_e}\left\{\frac{\partial p_e}{\partial s} + \eta n_e k_B \frac{\partial T_e}{\partial s}\right\} \\ = -\frac{1}{eAn_e}\left\{(1+\eta)\left[\frac{\partial}{\partial s}\left(Ap_e\right) - Ap_e\frac{\partial \ln A}{\partial s}\right] - \eta k_B T_e\left[\frac{\partial}{\partial s}\left(An_e\right) - An_e\frac{\partial \ln A}{\partial s}\right]\right\}, \tag{22}$$

where

$$\eta \equiv \frac{m_e}{p_e}\left(\frac{3}{5}\sum_i \nu_{ei} + \sum_n \nu_{en} z_{en}\right)\frac{\kappa_e}{k_B} \tag{23}$$

is a dimensionless number which characterizes the relative importance of the electron thermal diffusion effect. This work only concerns situations where the low-altitude thermal electron velocities are relatively small. Proper consideration of situations where this is not true, such as in auroral downward current regions, would require the retention of additional collisional terms involving electron-ion and electron-neutral friction.

This expression for the ambipolar electric field does not explicitly contain any moments of the suprathermal electron distribution, and yet the model will still capture the augmentation of the ambipolar electric field by suprathermal electrons. The study by *Khazanov et al.* [1997] also only used the thermal electron pressure gradient to set the ambipolar electric field, and yet those authors were able to demonstrate significant augmentation of the ambipolar electric field by photoelectrons. As shown in Appendix B, (22) is a limiting case of (B7). Furthermore, (B7) and the steady state suprathermal electron transport equation, (13), together imply (B6). Intuitively, (B6) shows that the ambipolar electric field is driven by pressure gradients in both the thermal and suprathermal electron gasses. The suprathermal electrons affects u_e through the current continuity condition, and u_e affects p_e in the electron energy equation. The thermal electron pressure will adjust itself such that (B6) is always satisfied even though this equation is never explicitly used.

2.5. Numerical Methods

The model uses two different time steps: an outer step size which is fixed at 180 s and an inner step size which adjusts itself using a Courant condition based on the ion dynamics and is typically ~0.2 s. The above equations are all in the limit of small electron mass, so even smaller time scales associated with the thermal electron dynamics, such as the inverse plasma frequency and the suprathermal electron travel times, do not need to be considered. Once per outer time step the NRLMSISE-00 model is called to update the neutral atmosphere, the photoproduction routine is called to update the ion and photoelectron production rates, and the steady state suprathermal electron transport solver is called to update the suprathermal electron distribution moments, the thermal electron heating rates, and the secondary production rates. The photoproduction routine only depends on the neutral atmospheric parameters and the solar spectrum, so it only needs to be called as often as NRLMSISE-00 is called. The suprathermal electron transport, however, does depend on the thermal electron parameters and the electric fields as well as the neutral atmospheric parameters and the solar spectrum. Nonetheless, as long as the thermal electron densities and electric fields are not changing rapidly compared to the outer time scale, updating the suprathermal electron parameters at the outer time scale will not introduce serious errors and is much more computationally efficient than calling the suprathermal electron solver at the inner time scale. This approach is not appropriate for studying the suprathermal electron effects on polar wind shocks and other transients, but it is sufficient for studying quasi steady state solutions.

Once the ion primary and secondary production rates, the thermal electron heating rates, and the suprathermal electron densities and net fluxes are specified, (1)–(4) and (20) form a closed system of equations for the ion densities, ion fluxes, ion energy densities, ion heat fluxes, and electron energy densities. Many of the collisional terms in these equations vary by orders of magnitude over the domain and thus must be treated implicitly. However, many of the transport terms are both nonlinear and involve derivatives of state variables, meaning these terms are most easily treated explicitly. A simple solution is to split the system of equations into two simpler systems and use operator splitting [cf. *LeVeque*, 2002, chapter 17]. Every inner time step involves an implicit time step of the first system followed by an explicit time step of the second system. The step size for both of these steps is the inner time scale (~0.2s).

The explicit numerics system is

$$\frac{\partial}{\partial t}\left(An_i\right)+\frac{\partial}{\partial s}\left[An_iu_i\right]=0 \tag{24}$$

$$\frac{\partial}{\partial t}\left(An_iu_i\right)+\frac{\partial}{\partial s}\left[An_iu_i^2+A\frac{p_i}{m_i}\right]=\frac{A}{m_i}n_ieE_\parallel+\frac{A}{m_i}p_i\frac{\partial \ln A}{\partial s} \tag{25}$$

$$\frac{\partial}{\partial t}\left(\frac{A}{m_i}\epsilon_i\right)+\frac{\partial}{\partial s}\left[\frac{A}{m_i}\left(u_i\epsilon_i+u_ip_i+q_i\right)\right]=\frac{A}{m_i}n_iu_ieE_\parallel \tag{26}$$

$$\begin{aligned}\frac{\partial}{\partial t}\left(\frac{A}{m_i}q_i\right)+\frac{\partial}{\partial s}\left[\frac{16}{5}\frac{A}{m_i}u_iq_i\right]&=\frac{11}{5}u_i\frac{\partial}{\partial s}\left(\frac{A}{m_i}q_i\right)-\frac{5}{3}v_{Ti}^2\frac{\partial}{\partial s}\left(\frac{A}{m_i}\epsilon_i\right)+\frac{5}{3}v_{Ti}^2u_i\frac{\partial}{\partial s}\left(An_iu_i\right)\\&+\left(\frac{5}{2}v_{Ti}^4-\frac{5}{6}v_{Ti}^2u_i^2\right)\frac{\partial}{\partial s}\left(An_i\right)-\frac{2}{5}\frac{A}{m_i}u_iq_i\frac{\partial \ln A}{\partial s}\end{aligned} \tag{27}$$

$$\frac{\partial}{\partial t}\left(\frac{3}{2}Ap_e\right)+\frac{\partial}{\partial s}\left[\frac{5}{2}\left(u_e+\tilde{u}_e\right)p_e\right]=-An_eu_eeE_\parallel. \tag{28}$$

When (22) is substituted for the ambipolar electric field, these equations are in the form

$$\frac{\partial \mathbf{W}}{\partial t}+\frac{\partial \mathbf{F}}{\partial s}-\mathbf{L}\frac{\partial \mathbf{W}}{\partial s}-\mathbf{S}=\mathbf{0}, \tag{29}$$

where **W** is a 13-element vector of state variables (three ions times four ion parameters plus thermal electron energy density), **F** is a 13-element vector of fluxes, **S** is a 13-element vector of sources, and **L** is a 13 by 13 sparse matrix. All of these quantities can be computed from the state variables without needing derivatives of the state variables.

Kőrösmezey et al. [1993] have shown that the sixteen-moment transport equations can also be written in the form of (29) and discussed one possible finite volume scheme for systems of this form. This work uses a simpler finite volume scheme which is only second-order accurate in space but never requires the computation of characteristic speeds from eigenvalue solvers and never couples the source terms between adjacent cells.

First, given the cell averages of the state variables after the most recent implicit step, values of these state variables on the left and right sides of the cell interfaces are reconstructed using a van Leer slope limiter [*LeVeque*, 2002]. If $\overline{\mathbf{W}}_i$ is the cell average in cell i and σ_i is the slope determined from the slope limiter for the reconstruction in cell i, then the value immediately below the interface between cells i and $i+1$ is $\mathbf{W}_{i+1/2}^- = \overline{\mathbf{W}}_i + \frac{1}{2}\sigma_i\Delta s_i$, and the value immediately above the interface is $\mathbf{W}_{i+1/2}^+ = \overline{\mathbf{W}}_{i+1} - \frac{1}{2}\sigma_{i+1}\Delta s_{i+1}$. Next, the local Lax-Friedrichs fluxes are constructed at the cell interfaces [*LeVeque*, 2002]

$$\mathbf{F}_{i+1/2}=\frac{1}{2}\left[\mathbf{F}\left(\mathbf{W}_{i+1/2}^-\right)+\mathbf{F}\left(\mathbf{W}_{i+1/2}^+\right)-\mathbf{a}_i\left(\mathbf{W}_{i+1/2}^+-\mathbf{W}_{i+1/2}^-\right)\right]. \tag{30}$$

The matrix $\mathbf{a}_i$ is a diagonal matrix containing the freezing speeds. *Palmadesso et al.* [1988] and *Kőrösmezey et al.* [1993] have discussed the characteristic speeds of the sixteen-moment equations in detail. Like the sixteen-moment equations, the eight-moment equations contain ion-thermal waves which travel approximately at the ion thermal speed and ion-acoustic waves which travel somewhat faster than ion acoustics waves would in an isothermal or adiabatic ion gas. Instead of computing the exact characteristic speeds from an eigenvalue solver, the model simply sets the freezing speeds for fluxes related to ion j to

$$a^j=\left|u_j\right|+2\sqrt{\frac{p_j}{n_jm_j}+\frac{p_e}{n_em_j}} \tag{31}$$

where the ad hoc factor of 2 virtually always causes these speeds to be slightly faster than the corresponding characteristic speeds. The freezing speed for the electron energy equation is

$$a^e=\left|u_e+\frac{5}{3}\tilde{u}_e\right|. \tag{32}$$

The freezing speeds are evaluated using the reconstructed values on both sides of the interface and the faster results are used in the flux evaluation. Furthermore, at the beginning of each inner time step the various freezing speeds are evaluated using the cell averages from the end of the last time step and the results are uses to determine the new time step according to

$$\Delta t=\min_i\left\{\frac{\Delta s_i}{2a_i^e},\min_j\frac{\Delta s_i}{2a_i^j}\right\}. \tag{33}$$

The H^+ freezing speed virtually always determines the time step.

The third term in (29) requires derivatives of the state variables. These are computed from the reconstructed values at the cell interfaces using

$$\left.\frac{\partial \mathbf{W}}{\partial s}\right|_i \approx \frac{1}{2\Delta s_i}\left[\mathbf{W}^+_{i+1/2} + \mathbf{W}^-_{i+1/2} - \mathbf{W}^+_{i-1/2} - \mathbf{W}^-_{i-1/2}\right]. \tag{34}$$

Finally, $\mathbf{L}_i$ and $\mathbf{S}_i$ are evaluated using the cell averages and the time advance equation is

$$\overline{\mathbf{W}}_i^{n+1} = \overline{\mathbf{W}}_i - \frac{\Delta t}{\Delta s_i}\left[\mathbf{F}_{i+1/2} - \mathbf{F}_{i-1/2}\right] + \Delta t \mathbf{L}_i \left.\frac{\partial \mathbf{W}}{\partial s}\right|_i + \Delta t \mathbf{S}_i \tag{35}$$

The implicit numerics system could be written in terms of the same state variables as the explicit numerics system, but it is more compactly expressed and better conditioned in terms of a different set of variables:

$$\frac{\partial n_i}{\partial t} = P_i - L_i' n_i \tag{36}$$

$$\frac{\partial u_i}{\partial t} = \frac{1}{n_i m_i}\frac{\delta M_i}{\delta t} - g \tag{37}$$

$$\frac{\partial T_i}{\partial t} = \frac{2}{3}\frac{1}{k_B n_i}\frac{\delta E_i'}{\delta t} \tag{38}$$

$$\frac{\partial}{\partial t}\left(\frac{q_i}{n_i m_i}\right) = \frac{1}{n_i m_i}\frac{\delta q_i'}{\delta t} - \frac{q_i}{n_i^2 m_i}\frac{\delta n_i}{\delta t} \tag{39}$$

$$\frac{\partial T_e}{\partial t} = \frac{2}{3}\frac{1}{k_B n_e}\left[\frac{\delta E_e'}{\delta t} + \frac{1}{A}\frac{\partial}{\partial s}\left(A\kappa_e \frac{\partial T_e}{\partial s}\right)\right] \tag{40}$$

All of the ion equations do not involve any spatial derivatives and thus can be solved one cell at a time. The electron temperature equation only involves spatial derivatives of the electron temperature, and thus only requires a simple tridiagonal linear system solve. The nonlinear expressions for the electron thermal conductivity, reaction rates, collision frequencies, heating and cooling rates, and correction factors ψ and ϕ are all evaluated using the old values of the state variables. The densities are updated first. Then the ion velocities and heat flows are updated together in a six by six linear system solve at each grid cell. Finally, the ion and electron temperatures are updated using the updated densities and velocities. This order of operations avoids the need for nonlinear implicit solvers and also guarantees that the total work done by ion-ion collisions equals the total heat created by the ion-ion frictional heating terms.

2.6. Boundary Conditions

In the implicit numerics portion of the fluid model only the electron temperature equation involves spatial derivatives. The lower boundary condition is that $T_e = T_n$. The upper boundary condition is an imposed electron temperature gradient. In the simulations where this gradient is nonzero, it is varied in such a way that the contribution to the total electron heat flux from this gradient, $q_{e;\nabla T_e} = -\kappa_e \nabla T_e$, is constant.

The explicit numerics portion of the fluid model uses two ghost cells at each boundary to set the boundary conditions. At the lower boundary of the model, transport processes are negligible compared to local production/loss and heating and cooling. Thus, the bottom of the model uses a "hard wall" boundary condition. In the lower ghost cells the fluxes and heat fluxes are set to zero in the ghost cells and the densities and energy densities are populated using zero order extrapolation from the last real cell. Outflow conditions are used at the upper boundary. All of the ion parameters in the upper ghost cells are filled with zero-order extrapolation from the last real cells, which is tantamount to

$$\left.\frac{\partial}{\partial s}\left(An_i\right)\right|_{s_{UB}} = \left.\frac{\partial}{\partial s}\left(An_i u_i\right)\right|_{s_{UB}} = \left.\frac{\partial}{\partial s}\left(\frac{A}{m_i}\epsilon_i\right)\right|_{s_{UB}} = \left.\frac{\partial}{\partial s}\left(\frac{A}{m_i}q_i\right)\right|_{s_{UB}} = 0. \tag{41}$$

If the ion velocities are negative, then this boundary condition will allow ion density to fill the model as if from an infinite high-altitude reservoir. To prevent this from happening, if the velocity is negative, then the fluxes in the ghost cells for that species are set to zero. This is normally the case for O^+ and rarely the case for the light ions. The electron pressure in the upper ghost cells is determined by assuming

$$\frac{\partial}{\partial s}\left(Ap_e\right) = k_B T_e \frac{\partial}{\partial s}\left(An_e\right) + An_e k_B \frac{\partial T_e}{\partial s}, \quad \left.\frac{\partial}{\partial s}\left(An_e\right)\right|_{s_{UB}} = 0, \tag{42}$$

and using the same electron temperature gradient which was used at the upper boundary of the implicit solver.

In the suprathermal electron transport solver the lower boundary is treated as described by *Varney et al.* [2012]; local equilibrium is assumed below 120 km and no upward flux is allowed to cross the boundary at 120 km. The upper boundary condition on the upward fluxes is simply

$$\frac{\partial}{\partial s}\left(A\Phi\right)\Big|_{s_{UB}} = 0, \tag{43}$$

while the downward fluxes at the upper boundary must be specified. Two different populations of downward moving suprathermal electron are considered at the upper boundary: polar rain (i.e., soft precipitation of solar wind origin) and reflected photoelectrons.

The reflected photoelectrons are modeled by specifying a potential energy difference between the upper boundary and infinity, $\mathcal{E}_r$, and assuming that beyond the upper boundary the motion of suprathermal electrons is collisionless and adiabatic. All upward moving photoelectrons with energies less than $\mathcal{E}_r$ will reflect. A small portion of the upward moving photoelectrons with energies greater than $\mathcal{E}_r$ can also reflect if they leave with pitch angles greater than zero, but the size of this population goes to zero in the limit where the potential structure is infinitely far away. Ignoring that population is tantamount to assuming the loss cone has become infinitesimal by the altitude of the potential drop.

In the absence of reflection potentials, the polar rain flux is assumed to have a Maxwellian energy distribution and to travel in a narrow loss cone. For polar rain with total number flux Γ_R, characteristic energy $\mathcal{E}_0$, and total energy flux $2\Gamma_R\mathcal{E}_0$ the flux is

$$\Phi_R\left(\mathcal{E},\mu;\Gamma_R,\mathcal{E}_0\right) = \frac{\Upsilon(\mu)}{\pi}\frac{\Gamma_R}{\mathcal{E}_0}\frac{\mathcal{E}}{\mathcal{E}_0}\exp\left[-\frac{\mathcal{E}}{\mathcal{E}_0}\right], \tag{44}$$

where $\int_{-1}^{0}\Upsilon(\mu)\,\mathrm{d}\mu = 1$. The pitch angle distribution factor, $\Upsilon(\mu)$, is assumed to be so narrow that all of the precipitating electrons appear in the μ bin closest to $\mu = -1$. If a potential structure exists which reflects photoelectrons back into the ionosphere, the same structure will accelerate, precipitating polar rain electrons. In the limit where the loss cone is infinitesimal at the altitude of the potential structure, the potential simply shifts (44) up by $\mathcal{E}_r$. The corresponding energy flux of the shifted distribution is $\Gamma_R\left(2\mathcal{E}_0+\mathcal{E}_r\right)$. The complete downward flux at the upper boundary is given by

$$\Phi\left(s_{UB},\mathcal{E},\mu\right) = \begin{cases} \Phi\left(s_{UB},\mathcal{E},-\mu\right) & \mathcal{E}\le\mathcal{E}_r \\ \Phi_R\left(\mathcal{E}-\mathcal{E}_r,\mu;\Gamma_R,\mathcal{E}_0\right) & \mathcal{E}>\mathcal{E}_r. \end{cases} \tag{45}$$

The reflection potential has no effect on the upper boundary condition for the ions. This assumption is justified if the potential structure is high enough in altitude for the plasma to be dominated by H^+ and for the H^+ to be supersonic. In this case a sharp drop in the H^+ density and a sharp increase in the H^+ velocity will appear at the location of the potential structure [cf. *Barakat et al.*, 1998b]; however, information about these discontinuities cannot be transmitted down the field line because the characteristic velocities in a supersonic gas all point upward.

3. Example Results

As an example, Figure 1 summarizes the state of a reference simulation performed for a field line located over Resolute Bay, Canada (74.73°N, 94.91°W geographic) at 1800 UT on the June solstice for medium-high solar conditions ($F_{10.7} = 140$) and quiet geomagnetic conditions ($Ap = 3.0$). The simulation was initialized 36 h before the time shown. In June this location is continuously sunlit. The first 6 h of the simulation exhibit transient behavior associated with the initial conditions, but the rest of the simulation exhibits a quasi steady state which slowly changes with the changes in the solar zenith angle. This simulation was performed with zero polar rain, zero electron heat flux down from the upper boundary, zero FAC, and a constant reflection potential of 40 eV. Figure 1 (first panel) shows the densities of thermal electrons (e_t^-), suprathermal electrons (e_s^-), and the three transported ion species. As expected for the sunlit polar cap, O^+ is the dominant ion at all altitudes below 1 R_E [cf. *Kitamura et al.*, 2011; *Glocer et al.*, 2012].

Figure 1 (second panel) shows several different velocities. Solid lines are used for the fluid velocities of the species, dashed lines are used for the ion acoustic speeds, $c_{si} = \sqrt{\frac{p_i}{n_i m_i}+\frac{p_e}{n_e m_i}}$, and dash-dotted lines are

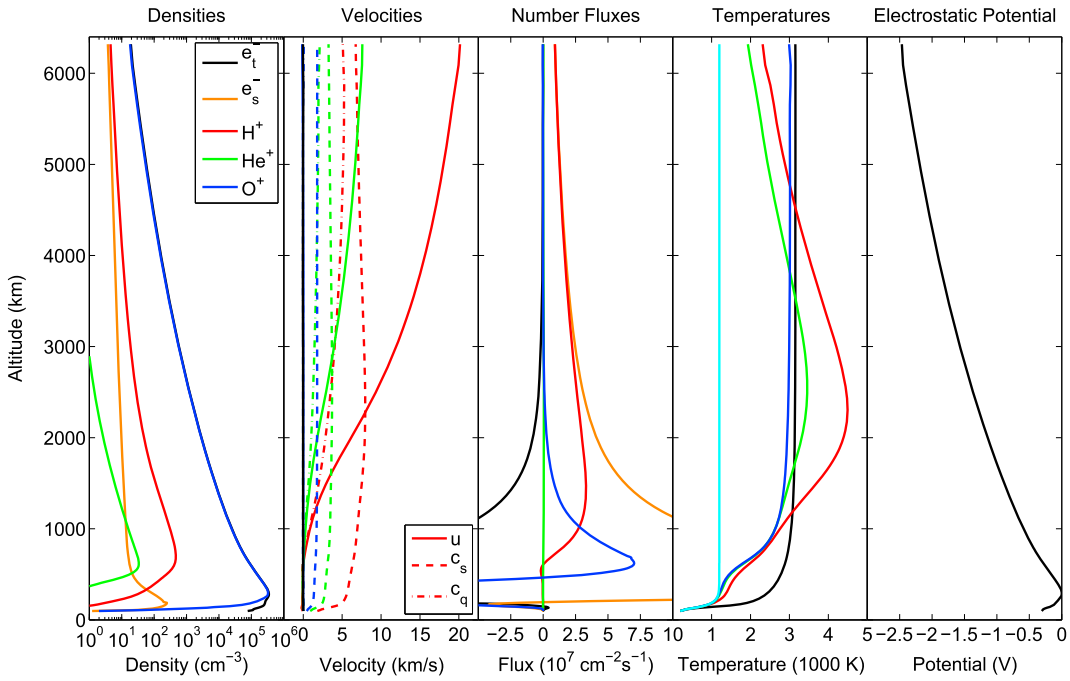

Figure 1. Summary of the reference simulation. (first to fifth panels) The panels plot the densities, velocities, number fluxes, temperatures, and electrostatic potential. The density curves labeled e_t^- and e_s^- represent the densities of thermal and suprathermal electrons, respectively. In the velocities panel solid lines are used for fluid velocities, dashed lines are used for ion acoustic speeds, and dash-dotted lines are used for heat flow velocities (see text). In the temperature panel the cyan curve is the NRLMSISE-00 neutral temperature. The electrostatic potentials in the right panel have been shifted such that their maximum value is zero.

used for "heat flow velocities," defined as $c_{qi} = \frac{q_i}{p_i}$. The H^+ and He^+ ion flows become supersonic at 2300 and 2900 km, respectively, whereas the O^+ velocities remain insignificant at all altitudes. When the heat flow velocity is much less than the fluid velocity, the behavior is essentially adiabatic. In this simulation the ion heat flow velocities are generally less than both the fluid velocities and the ion acoustic speeds but are nonetheless on the same order of magnitude. Thus, while the heat flows are not the dominant terms in the ion energy equations, the flows are not adiabatic either.

For the conditions of the reference simulation the thermal electron fluxes at the upper boundary are nearly zero. The applied reflection potential of 40 eV is crucial for the simulation to achieve zero current without requiring huge thermal electron inflows through the upper boundary. In the uppermost real computational cell the thermal electron flux is -7×10^4 cm^{-2} s^{-1}, the upward suprathermal electron flux is 2.5154×10^8 cm^{-2} s^{-1}, the downward (reflected) suprathermal electron flux is -2.4244×10^8 cm^{-2} s^{-1}, the net suprathermal electron flux is 9.10×10^6 cm^{-2} s^{-1}, the H^+ ion flux is 9.12×10^6 cm^{-2} s^{-1}, the He^+ ion flux is 1.5×10^5 cm^{-2} s^{-1}, and the O^+ is -2.4×10^5 cm^{-2} s^{-1}. The potential reflects most of the escaping photoelectrons back into the ionosphere, and the net flux carried by the highest-energy photoelectrons is primarily balanced by the H^+ ion outflow. The O^+ fluxes are small because O^+ is nearly in diffusive equilibrium, and the He^+ fluxes are small despite the supersonic He^+ velocities because the He^+ densities are so small.

Figure 1 (fourth panel) shows the temperatures of the thermal electrons, the three transported ion species, and the NRLMSISE-00 neutral temperature. The electrons become nearly isothermal at high altitudes as expected when the top boundary condition is zero temperature gradient. The O^+ ion temperatures equal the neutral temperature at low altitudes, then approach but never reach the electron temperatures at high altitudes. The O^+ heat flows have the opposite sign from the O^+ temperature gradients as expected from Fourier's law. The temperatures and heat flows of the light ions, however, exhibit much more complicated behavior because these minor ions are flowing at supersonic speeds through the dominant ion gas. This relative motion induces significant heat flows in the light ion gases via the collisional terms involving velocity differences in (7). Effects associated with these collision terms are known as diffusion thermal effects [*Schunk and Nagy*, 2009]. The light ion heat flows are upward at most altitudes, even if the temperature gradients

are upward, as a result of diffusion thermal effects [cf. *Blelly and Schunk*, 1993, Figure 4d]. Of the two velocity correction terms for Coulomb collisions, ψ_{ij} goes to zero with increasing relative velocity much faster than ϕ_{ij} [*Schunk*, 1977]. Thus, Coulomb collisions are ineffective at equalizing the ion temperatures when supersonic velocity differences exist, but frictional heating can still be important. The combination of ion-ion frictional heating and upward induced heat flows in the ion gases causes the light ion temperatures to exceed the electron temperatures around the sonic points. These high light ion temperatures are very effective at driving light ion outflow. At the highest altitudes where the plasma is collisionless the light ions are cooled by adiabatic expansion due to increasing flux tube area and increasing velocity with altitude.

Finally, Figure 1 (fifth panel) shows the electrostatic potential associated with the ambipolar electric fields. The potential drop between the peak of the *F* region and the top boundary is 2.49 V. *Khazanov et al.* [1997] have presented collisionless kinetic simulations of the polar wind between 500 km and 5 R_E with various different densities of photoelectrons at their lower boundary. They estimate potential drops of 2.87 and 7.25 V between 500 km and 5 R_E for photoelectron fractions of 0.01% and 1.00%, respectively, with most of these potential drops occurring in the lowest 2–3 R_E. The potential drops computed from these collisionless simulations should be regarded as upper bounds for what photoelectrons can do. Their simulations look like classical polar wind solutions for photoelectron fractions less than ~0.05%, but then transition to another regime where the O^+ outflows supersonically as the photoelectron fraction approaches 1.00%. They note that photoelectron fractions above 0.10% are rare, and thus, this other regime represents an unusual extreme case. *Khazanov et al.* [1998] generalized the work of *Khazanov et al.* [1997] to allow for arbitrary potential profiles, including nonmonotonicities. According to *Khazanov et al.* [1998], the results of *Khazanov et al.* [1997] hold at low and moderate photoelectron concentrations, but the generalized model produces substantially different potential profiles and more outflow compared to the *Khazanov et al.* [1997] model when the photoelectron fraction at 500 km is 0.03% or higher. For the reference simulation in Figure 1 the photoelectron fraction at 500 km is 0.0143%, and thus, this simulation lies comfortably in the classical polar wind regime. The potential drops associated with the ambipolar electric field are much too small to explain the assumed 40 V drop above the upper boundary. This drop must be mostly associated with some other kind of potential structure such as double layers like those simulated by *Wilson et al.* [1997] and *Su et al.* [1998].

3.1. Effects of Different Types of Energy Flows

A strength of the model developed for the present paper is it can take three different forms of energy flow through the upper boundary: thermal electron conduction, polar rain, and reflected photoelectrons. Applying the same amount of energy through different channels results in different signatures in the ionosphere, thus permitting a discussion of the possible nature of this energy flow instead of just an estimation of its numerical value. Figure 2 summarizes the results of 14 simulations with different amounts and kinds of energy flux applied at the upper boundary. All examples shown are for the same time, location, and conditions as the reference simulation in Figure 1. Note, unless otherwise specified, all these simulations use a 40 eV reflection potential. The left column shows the thermal electron velocities, the middle column shows the thermal electron densities, and the right column shows the electron and O^+ ion temperatures. The top row shows the effects of changing the reflection potential, the second row shows the effects of various fluxes of 50 eV characteristic energy polar rain, and the third row shows the effects of various electron temperature gradients at the upper boundary. In each row the red curves are the reference simulation.

The three kinds of energy flow all influence the electron temperatures above ~300 km and the ion temperatures above ~750 km and are thus hard to differentiate from temperature measurements alone. In the simulations with thermal electron heat conduction through the upper boundary the electron temperature profiles at high altitude increase as $s^{2/7}$ which is expected when the thermal conductivity is proportional to $T_e^{5/2}$ [*Schunk and Nagy*, 2009]. When the energy flux is applied through only suprathermal electron processes, however, the roughly isothermal nature of the high-altitude electrons is retained.

The interpretation of the effects of suprathermal electrons coming down from the upper boundary is complicated because they carry number fluxes as well as heat fluxes and thus influence the thermal electron velocities through the current continuity condition. Reflection potentials less than the reference value of 40 eV require significant thermal electron inflows to achieve zero current, with the required inflow velocity exceeding 65 km/s in the case of zero reflection potential. Even if a sufficient population of cold elec-

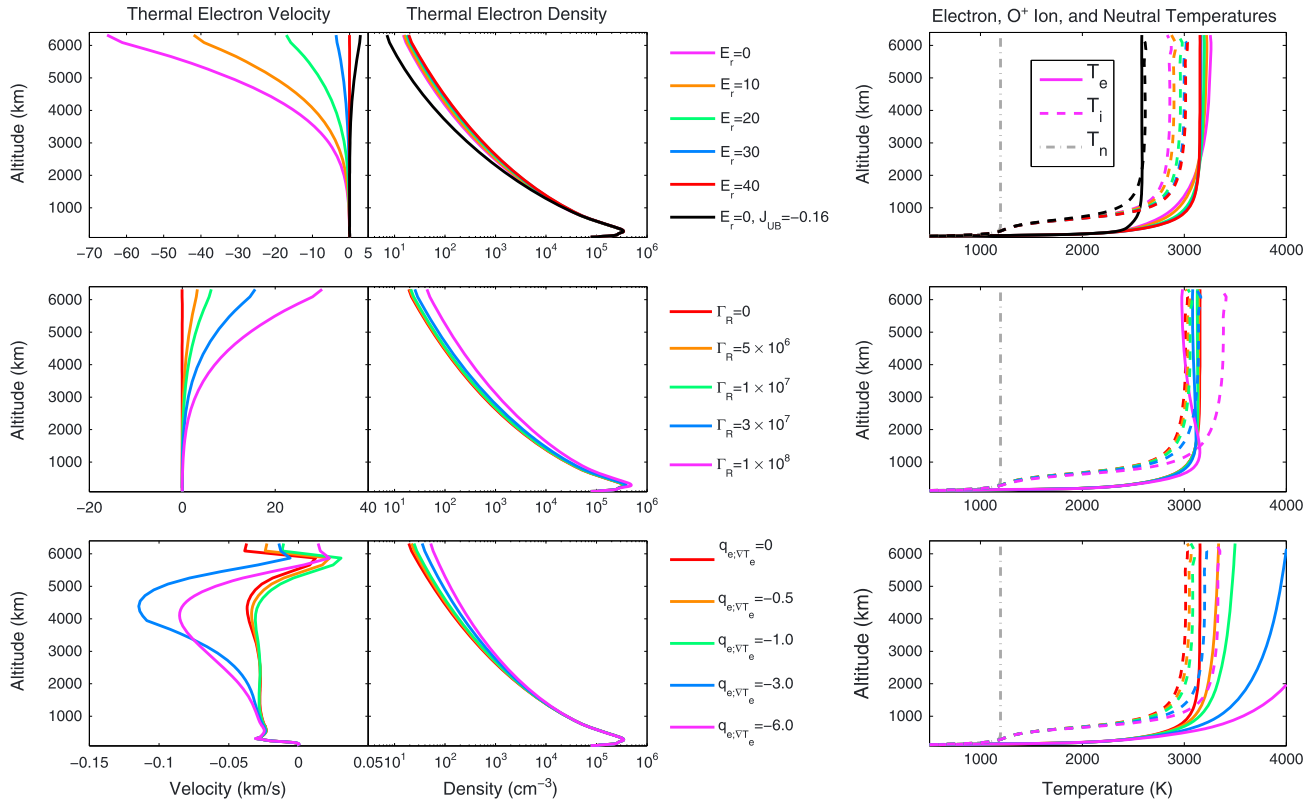

Figure 2. Summary plots of simulations with parameters changed from the reference case. (first to third rows) The rows illustrate the effects of changing the reflection potential, polar rain flux, and the electron heat flux associated with a temperature gradient at the upper boundary. The colors in the legends apply to the entire row. The temperature panels use solid lines for electron temperature, dashed lines for O^+ temperatures, and dash-dotted lines for neutral temperatures. The legends quote reflection potentials E_r in eV, FAC densities at the upper boundary J_{UB} in μA m^{-2} (negative = downward), polar rain fluxes at the upper boundary Γ_R in cm^{-2} s^{-1}, and the electron heat fluxes associated with temperature gradients at the upper boundary $q_{e;\nabla T_e}$ in 10^8 eV cm^{-2} s^{-1} (negative = downward). The polar rain simulations all use a characteristic energy of 50 eV and a reflection (acceleration) potential of 40 eV, and thus, the corresponding energy fluxes in eV cm^{-2} s^{-1} are $140\Gamma_R$.

trons existed at high altitudes to support this inflow, such large velocity differences between the ions and electrons could potentially excite instabilities.

As expected, the effect of decreasing the reflection potential is to decrease the electron temperatures at low altitudes since more photoelectrons escape without thermalizing. The electron temperatures above ~2300 km, however, go up with decreasing reflection potential. Even though the energy flux associated with the reflected photoelectrons decreases with decreasing reflection potential, the inflowing thermal electrons carry a downward energy flux as well. The large electron inflows heat the electrons via adiabatic compression. In the simulation with no reflection potential the energy flux at the upper boundary associated with the inflow is $\frac{5}{2}u_e p_e = -6.83 \times 10^7$ eV cm^{-2} s^{-1}. Temperature is a measure of energy per particle, and thus, the temperature decreases at low altitudes where the densities are large represent a much larger energy change than the temperature increases at high altitudes. Let the flux tube averaged electron energy density be defined as

$$\langle W_e \rangle = \frac{1}{A_{UB}} \int_{s_{LB}}^{s_{UB}} A(s) n_e(s) k_B T_e(s)\, \mathrm{d}s. \tag{46}$$

For the simulations from Figure 2 (first row), this number is 463, 471, 485, 497, and 503 GeV cm^{-2} for reflection potentials of 0, 10, 20, 30, and 40 eV, respectively. Reducing the number of reflected photoelectrons and replacing them with the same number flux of thermal inflow has the effect of lowering $\langle W_e \rangle$, which is expected since the thermal inflow has a lower average energy per particle than the reflected photoelectrons. Thermal electron velocity effects also explain why the high-altitude electron temperatures decrease with the addition of polar rain. In these cases the upward electron velocities cool the electrons to lower temperatures than the ions via adiabatic expansion.

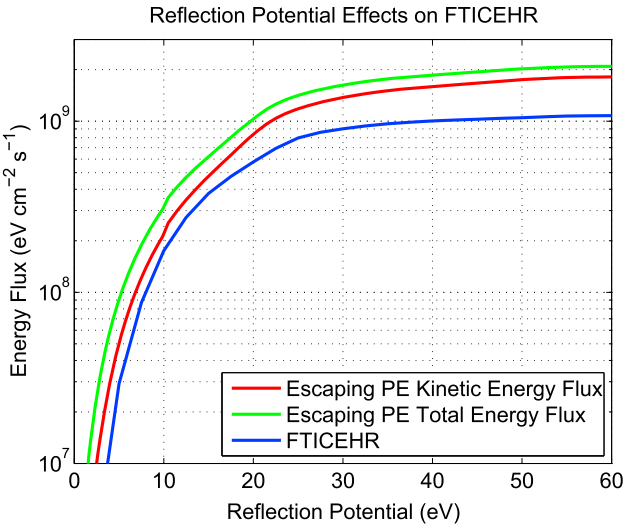

Figure 3. Cumulative escaping photoelectron kinetic energy fluxes (red), cumulative escaping photoelectron total energy fluxes (green), and FTICEHR as a function of reflection potential for the reference case. See the text for definitions of these quantities.

The black curves in Figure 2 (first row) are from a simulation where the reflection potential is set to zero but a FAC of -0.16 μA m^{-2} is assumed at the upper boundary. This downward current is primarily carried by escaping photoelectrons. The thermal electron velocities in the current carrying simulation are upward instead of downward and compared to the reference simulation the temperature at 1470 km is 529 K lower. This substantial temperature change is a meaningful indication of the importance of reflected photoelectrons in heating the thermal electrons because neither the reference case nor the simulation with a FAC is complicated by adiabatic compression effects. The $\langle W_e \rangle$ for this simulation is 434 GeV cm^{-2}. This is lower than any of the other simulations because this simulation has neither reflected photoelectrons nor energy carried by thermal electron inflow.

Adding a temperature gradient, a reflection potential, or polar rain are all ways to increase the electron energy density by modifying the upper boundary condition. In order to compare the relative effectiveness of these three methods, it is instructive to apply the operator $\frac{-1}{A_{UB}} \int_{s_{LB}}^{s_{UB}} ds$ to the steady state limit of the electron energy equation. The result is

$$-\frac{5}{2} u_e\left(s_{UB}\right) p_e\left(s_{UB}\right) - q_e\left(s_{UB}\right) + \frac{1}{A_{UB}} \int_{s_{LB}}^{s_{UB}} A\left(Q_{phe} - Q^*_{phe}\right) ds \tag{47}$$
$$= \frac{1}{A_{UB}} \int_{s_{LB}}^{s_{UB}} A \left\{ n_e u_e e E_{\parallel} + \frac{3}{2} k_B T_e \frac{\delta n_e}{\delta t} - Q^*_{phe} + \sum_i n_e \nu_{ei} 3 k_B \left(T_e - T_i\right) + \sum_n L'_{en} \left(T_e - T_n\right) \right\} ds,$$

where Q^*_{phe} is what the suprathermal electron heating rate would be if no reflection potential or polar rain were included, but the ambipolar electric field and thermal electron density profile remained the same. In the above, the electron velocity and heat flux are assumed to be zero at the lower boundary. The three terms on the left-hand side (LHS) of (47) represent ways the upper boundary conditions heat the thermal electrons, and comparing the relative magnitudes of these three terms gives an indication of the dominant process. Nonetheless, even if the LHS of this equation is identical for two cases, the resulting electron temperature profiles will not be identical because the terms on the right-hand side of the equation are not totally independent of the upper boundary conditions.

To quantify how well the reflected photoelectrons heat the electrons, the electron density, electron temperature, and ambipolar electric field profiles were fixed to the values from the end of the reference simulation (i.e., Figure 1), and the suprathermal electron transport solver was called with many different reflection potentials. The flux tube integrated changes in the electron heating rates (FTICEHR), i.e. the third term on the LHS of (47), are plotted as function of reflection potential in Figure 3. The FTICEHR are evaluated by numerically integrating the difference between the electron heating rate from the case in question, Q_{phe}, and the heating rate computed from the zero reflection potential case, Q^*_{phe}. Also plotted are the cumulative kinetic and total energy fluxes of the escaping photoelectrons from the zero reflection potential case, defined as

$$q_{kinetic}(\mathcal{E}) = \int_0^{\mathcal{E}} d\mathcal{E}'\, \mathcal{E}' \int_0^1 d\mu\, \mu \Phi\left(s_{UB}, \mathcal{E}', \mu\right), \tag{48}$$

$$q_{total}(\mathcal{E}) = \int_0^{\mathcal{E}} \mathrm{d}\mathcal{E}' \left(\mathcal{E}' - eU\right) \int_0^1 \mathrm{d}\mu \, \mu\Phi\left(s_{UB}, \mathcal{E}', \mu\right), \tag{49}$$

respectively, where the potential energy $-eU = 2.49$ eV for the state at the end of the reference simulation. The FTICEHR increase monotonically with reflection potential, but the rate of increase above 30 eV is small because the peak in the photoelectron differential energy flux distribution is around 20 eV. For the reference value of 40 eV the FTICEHR is 1.01×10^9 eV cm^{-2} s^{-1}, which is 54.3% of the cumulative total energy flux at 40 eV. The FTICEHR is necessarily less than the cumulative total energy flux because reflected photoelectrons can lose energy to the neutrals as well as to the thermal electrons.

The concept of a FTICEHR can also be used to evaluate the effectiveness of polar rain electrons. Let Q_{phe} be the heating rate with all populations of suprathermal electrons included, Q^*_{phe} be the heating rate with no polar rain and no reflection potential, and Q'_{phe} be the heating rate with no polar rain but with a reflection potential. Let the FTICEHR associated with just the reflected photoelectrons be

$$\text{FTICEHR(reflection)} \equiv \frac{1}{A_{UB}} \int_{s_{LB}}^{s_{UB}} A \left(Q'_{phe} - Q^*_{phe}\right) \mathrm{d}s, \tag{50}$$

the FTICEHR associated with just the polar rain be

$$\text{FTICEHR(polar rain)} \equiv \frac{1}{A_{UB}} \int_{s_{LB}}^{s_{UB}} A \left(Q_{phe} - Q'_{phe}\right) \mathrm{d}s, \tag{51}$$

and the total FTICEHR associated with all populations of suprathermal electrons coming from the upper boundary be the sum of the two, i.e.,

$$\text{FTICEHR(total)} \equiv \frac{1}{A_{UB}} \int_{s_{LB}}^{s_{UB}} A \left(Q_{phe} - Q^*_{phe}\right) \mathrm{d}s. \tag{52}$$

In the simulation from Figure 2 with a polar rain flux of 10^7 cm^{-2} s^{-1}, the precipitating electrons carry a kinetic energy flux of 1.40×10^9 eV cm^{-2} s^{-1} at the upper boundary, which is larger than the FTICEHR of the reflected photoelectrons, and yet the effect of this polar rain on the low-altitude temperatures is minimal. At energies higher than 100 eV the cross sections for electron impact ionization dominate, and thus, the polar rain electrons are much less efficient at heating the electrons than reflected photoelectrons. Figure 4 shows the FTICEHR for polar rain with a kinetic energy flux of 10^9 eV cm^{-2} s^{-1} as a function of characteristic energy. Like Figure 3, the tests in Figure 4 fix the electron density, electron temperature, and ambipolar electric field to the values from the end of the reference simulation for every characteristic energy. The first curve uses no reflection (acceleration) potential, and the second uses 40 eV. For the second curve the flux is normalized such that the kinetic energy flux is 10^9 eV cm^{-2} s^{-1} after the acceleration through the 40 eV potential.

Even with the extra energy gained from the ambipolar electric field, the FTICEHR of polar rain is roughly an order of magnitude smaller than the kinetic energy flux. The effectiveness of polar rain decreases with increasing characteristic energy for two reasons. First, higher-energy electrons penetrate to lower altitudes where the neutral densities are higher. Second, the relative importance of inelastic collisions with neutrals versus Coulomb collisions increases with increasing energy. One might expect the reflection potentials to increase the effectiveness of polar rain since they will reflect some backscattered particles which would otherwise escape without thermalizing. However, the reflection potentials also shift the polar rain spectrum up in energy, thus decreasing the effectiveness of the primary electrons.

4. Comparisons to RISR-N Measurements

All of the RISR-N data shown below were collected using the 11-beam mode originally described by *Bahcivan et al.* [2010, see their Table 1 for relevant radar parameters and their Figure 1 for the beam geometry]. This mode interleaves an alternating coded pulse (AC) for the *E* region and lower *F* region with an uncoded long pulse (LP) for the *F* region and topside. The data shown below is all LP data. The LP autocorrelation functions were integrated for 5 min and then fit for electron density, electron temperature, ion temperature, and line-of-sight velocity using ion-neutral collision frequencies computed from a Mass

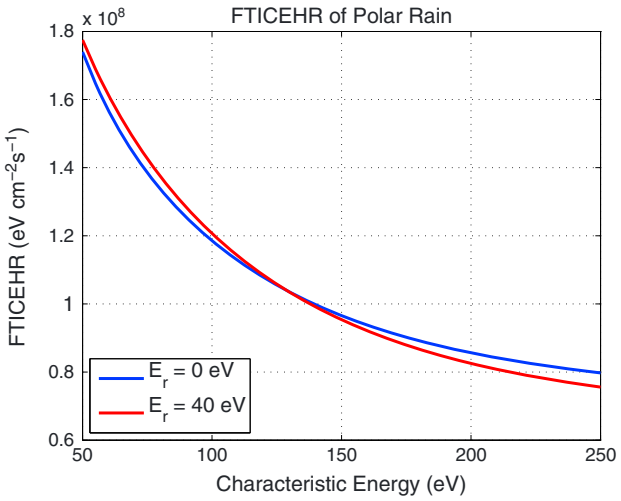

Figure 4. FTICEHR of polar rain with kinetic energy fluxes of 10^9 eV cm^{-2} s^{-1} at the top boundary as a function of characteristic energy. The reflection (acceleration) potentials used are indicated in the legend. Note that the peak differential energy flux of the polar rain occurs at $2\mathcal{E}_0$ and $2\mathcal{E}_0$ + 40 eV for the cases without and with the 40 eV potential, respectively. The peak photoelectron differential energy flux is at ~ 20 eV, and thus, the photoelectrons are comparable to 10 eV characteristic energy polar rain.

Spectrometer Incoherent Scatter (MSIS) neutral atmosphere and ion composition profiles taken from the model described in this paper. The data presented below is further postprocessed by interpolating the fitted parameters from the different beams onto a common altitude grid and averaging six of the 11 beams. The six beams chosen are the six highest elevation beams excluding the vertical beam (i.e., beams 4–9 in the notation of Figure 1 of *Bahcivan et al.* [2010]). The lower elevation beams do not reach very far above the peak of the *F* region, and the vertical beam is near the grating lobe limit of the phased array and thus has much lower gain and poorer signal-to-noise ratio. Due to the differing beam elevations, the data from different beams end at different maximum altitudes. Beams 4 and 6 end at 535 km, 5 ends at 570 km, 7 and 8 end at 602 km, and 9 ends at 654 km.

Figure 5 compares parameters from four different model runs to RISR-N data as a function of altitude at two different times. The top panels are for 2200 UT on 3 July 2012, and the bottom panels are for 1000 UT on 4 July 2012. The solar zenith angles at these two times are 59.0° and 76.2°, respectively. Figure 6 plots RISR-N data and parameters from the same four simulations at 529 km as functions of time. This altitude was chosen for comparison because it is the highest altitude with sufficiently reliable RISR-N data. The first model run shown uses (1) zero FAC, zero electron temperature gradient at the upper boundary, zero polar rain, and time-varying reflection potentials set using an automated method.

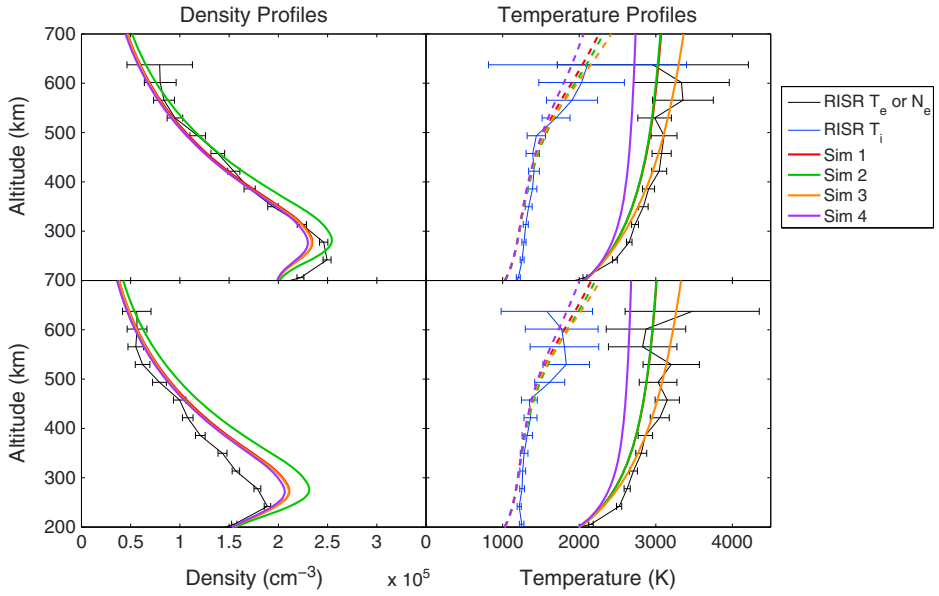

Figure 5. Plots of RISR-N fitted and modeled parameters for the four simulations described in the text. The red, green, orange, and purple lines correspond to simulations 1, 2, 3, and 4, respectively. The error bars represent two standard deviations. (right) The electron (solid lines) and O^+ ion (dashed lines) temperatures and (left) the electron densities. (bottom) For 2200 UT on 3 July 2012 and (top) for 1000 UT on 4 July 2012.

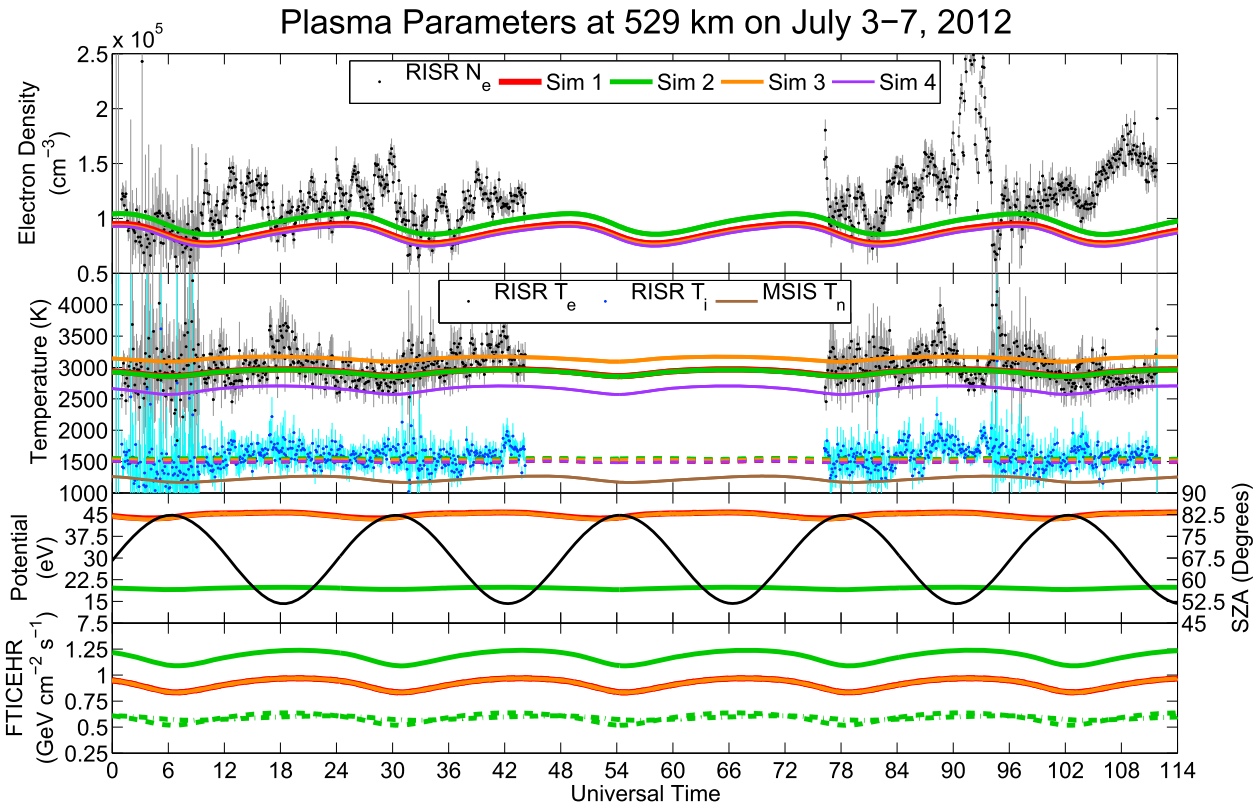

Figure 6. Various parameters from the four simulations for 3–7 July 2012 plotted at 529 km as functions of time. In each panel the red, green, orange, and purple lines correspond to simulations 1, 2, 3 and 4, respectively. (first panel) RISR-N measured electron density (black dots with gray two standard deviation error bars) and modeled electron density (solid lines). In this panel the red, orange, and purple lines on top of one another. (second panel) RISR-N measured electron (black dots with gray, two standard deviation error bars) and ion (blue dots with cyan, two standard deviation error bars) temperatures, modeled electron (solid lines) and O^+ ion (dashed lines) temperatures, and the MSIS neutral temperatures (brown line). In this panel the solid red and green lines on top of one another. (third panel) Solar zenith angle (black line, right ordinate) and the reflection potential (colored lines, left ordinate; the red and orange lines are on top of each other). (fourth panel) Total FTICEHR (solid lines), FTICEHR associated with reflected photoelectrons (dashed lines), and FTICEHR associated with polar rain (dash-dotted lines); the red and orange lines are on top of one another. Time 0 is 0 UT on 3 July 2012.

This variant of the code sets the reflection potential at each outer time step such that the absolute value of the cold electron velocity at the upper boundary is minimized. These automatically determined reflection potentials should be interpreted as the lower bound necessary to prevent cold electron inflow. The composition profiles from this first simulation were used to fit the RISR-N spectra. The other three simulations use (2) automatically determined reflection potentials and 50 eV characteristic energy polar rain with $\Gamma_R = 3 \times 10^7$ cm^{-2} s^{-1} at the upper boundary, (3) automatically determined reflection potentials and an electron temperature gradient associated with an electron heat flux of $q_{e;\nabla T_e} = -5 \times 10^8$ eV cm^{-2} s^{-1} at the upper boundary, and (4) no reflection potential and a FAC of $J_{UB} = -0.16$ μAm^{-2} at the upper boundary. Also plotted in Figure 6 are the automatically determined reflection potentials, the solar zenith angles (SZA), and the three different types of FTICEHR. In the automatic code, after the new reflection potential is determined the suprathermal electron transport solver is called two more times with polar rain disabled and with both reflection potentials and polar rain disabled. The heating rates from these extra calls are Q'_{phe} and Q^*_{phe}, respectively, and they are used to compute the three different types of FTICEHR. These FTICEHRs are never used by the model; they are simply diagnostics.

These four simulations also include two adjustments to the standard model that bring the electron density profiles into better agreement with the RISR-N measurements. First, the temperature dependence of NO^+ dissociative recombination reactions is assumed to be $T_e^{-0.5}$, following *Schunk and Nagy* [2009], instead of $T_e^{-0.85}$ as suggested by *Richards* [2011]. Both sources agree on rate at 300 K, but T_e in the F_1 region tends to be much greater than 300 K, so the temperature dependence matters. The modified exponent results in faster NO^+ dissociative recombination, and thus a much smaller F_1 region peak density. Second, the

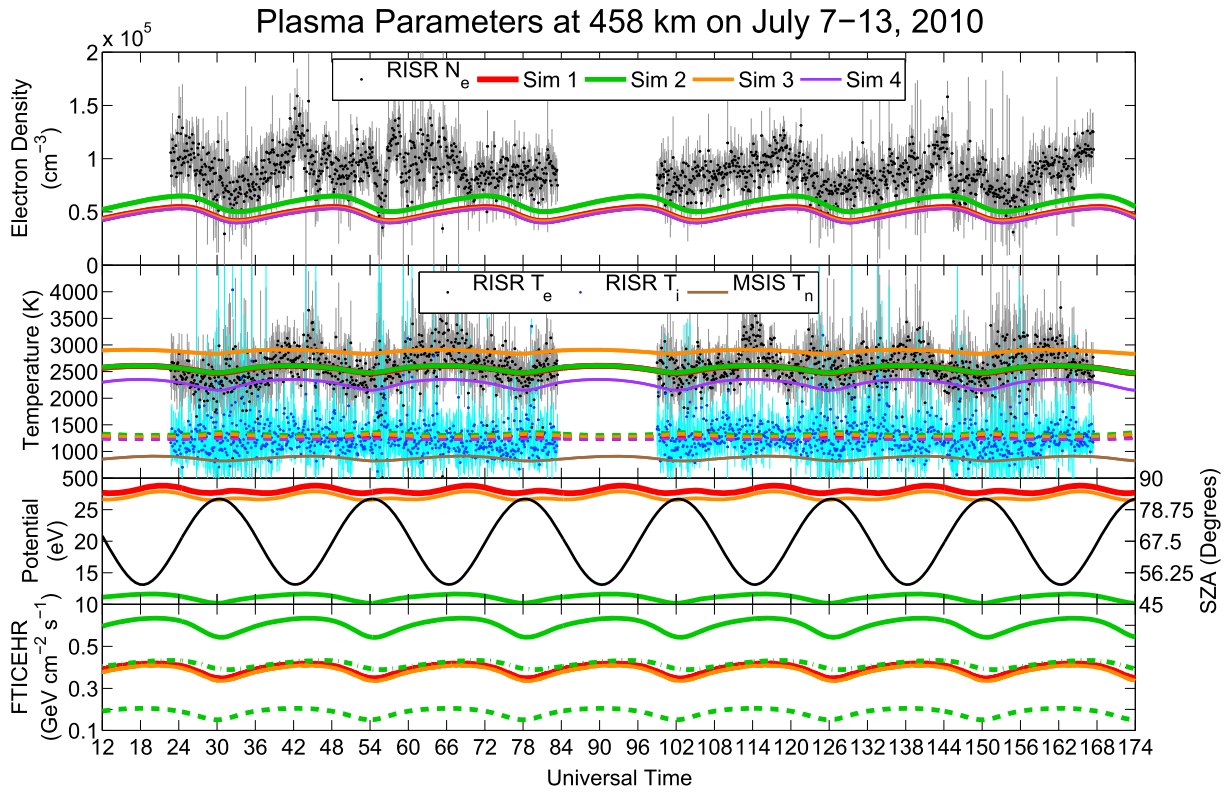

Figure 7. Measured and modeled plasma parameters at 458 km for 7–13 July 2010, presented in a similar format to Figure 6. Time 24 is 0 UT on 8 July 2010.

NRLMSISE-00 neutral O densities are multiplied by 0.8. This change lowers the F_2 region densities by ~20%. The NRLMSISE-00 climatology is known to have problems reproducing the O/N_2 ratios at auroral latitudes during the polar summer and during times of large geomagnetic activity [see *Hecht et al.*, 2012, and references therein]. To these authors' knowledge the reliability of NRLMSISE-00 composition in the summer polar cap has not been thoroughly examined. These two adjustments have significant effects on the electron density profiles but relatively small changes on the other parameters. The changes to the topside electron temperatures and automatically determined reflection potentials are ~50 K and ~3 eV, respectively.

The electron temperatures from simulation 4 are significantly lower than the RISR-N measurements in the topside, whereas the other three simulations show satisfactory agreement with the data. The electron temperatures in simulation 3 are higher than those in simulation 1, but by amounts which are comparable the error bars on the data. The automatically determined reflection potentials in simulation 2 are lower than those in simulations 1 and 3 because the polar rain flux partially balances the escaping photoelectron flux. Fewer reflected photoelectrons will lower the FTICEHR associated with the reflected photoelectrons, but the polar rain itself adds a FTICEHR. In this case the net result is an increase in the total FTICEHR when polar rain is included. Note that the FTICEHR associated with the polar rain of $\sim 6 \times 10^8$ eV cm^{-2} s^{-1} in simulation 2 is a fraction of the kinetic energy flux carried by the polar rain, $\sim 3.2 \times 10^9$ eV cm^{-2} s^{-1}, as expected from Figure 4. This extra FTICEHR does not translate into an increased temperature, however, because the polar rain also creates additional electron density via impact ionization. The increased electron density means the heat is divided among a larger number of electrons. The net effect is for electrons temperatures to decrease slightly with the addition of polar rain.

The simulations for Figure 6 were run using a daily $F_{10.7}$ index of 159.3 (the mean over this time period), an 81 day average $F_{10.7}$ index of 127, and an *Ap* index of 12.0 nT (which is median daily *Ap* over this time period). Thus, this example represents medium-high solar conditions and medium-low geomagnetic conditions. For comparison, Figure 7 presents RISR-N data and four simulations for 7–13 July 2010 using a daily $F_{10.7}$ index of 78.1, 81 day average $F_{10.7}$ index of 77.8, and an *Ap* index of 3.0 nT. A somewhat lower altitude was used for the comparison because of the decreased quality of the high-altitude data at lower solar flux conditions. The four simulations are identical to the four simulations presented for the July 2012 case

except for the solar conditions. Under these lower solar conditions the automatically determined reflection potentials and the FTICEHR associated with the reflected photoelectrons both decrease. Even though the polar rain number flux and characteristic energy are the same as in the higher solar conditions case, the FTICEHR associated with this polar rain is lower in this case because the reflection (acceleration) potential is lower. Nonetheless, the FTICEHR associated with this polar rain is approximately double of that associated with the reflected photoelectrons. In contrast, in the higher solar conditions case the two FTICEHRs are approximately equal.

5. Discussion

The statistical study by *Bekerat et al.* [2007] demonstrated that some form of heat flux into the high-latitude ionosphere usually exists. The polar cap examples presented in this paper are consistent with that conclusion. Simulations with no form of electron energy flux from the upper boundary consistently underestimate the electron temperatures compared to RISR-N measurements. Note these simulations must include a nonphysical downward FAC to remove the cold electron inflow and the energy flux associated with it. The IFM simulations performed by *Bekerat et al.* [2007] add heat fluxes by imposing a temperature gradient at the upper boundary, which is a standard practice in fluid modeling of the high-latitude ionosphere [*Ganguli*, 1996]. *Yau et al.* [1995] have argued that this practice is inconsistent with in situ measurements of the polar wind, however; the electron heat fluxes point upward and are associated with escaping photoelectrons. The simulations presented here without temperature gradients imposed at the upper boundary are all consistent with that observation. Even when reflection potentials are present, the total electron heat flux points upward due to the net escaping photoelectrons. Cases with a reflection potential have smaller upwards heat fluxes than cases without; the reflection potential causes the ionosphere to retain energy that it would otherwise lose. Simulations with reflected photoelectrons and simulations with both reflected photoelectrons and polar rain and no other source of heat from the upper boundary can satisfactorily reproduce RISR-N electron and ion temperature profiles in the 300–600 km region. The RISR-N measurements alone cannot prove that this extra heat is coming from suprathermal electrons and not thermal conduction because the two processes have very similar effects on the plasma temperatures in the 300–600 km region.

The model presented in this paper can heat the electrons using soft precipitation and reflected photoelectrons as well as temperature gradients imposed at the upper boundary. Soft precipitation and reflected photoelectrons are valid ways to transport energy in a collisionless plasma, and thus, simulations using only these two mechanisms to transport energy down from high altitudes are physically reasonable. The simulations with temperature gradients applied at the upper boundary, however, must be regarded with skepticism since temperature gradients are difficult to maintain as the plasma transitions to a collisionless limit. Assuming steady state, the electron heat flow is field aligned, and taking the limit of small electron mass, the general electron heat flow equation can be written as

$$\frac{k_B p_e}{m_e}\nabla T_e + \mathrm{HOT} = \frac{\delta q_e'}{\delta t}, \tag{53}$$

where the higher-order terms (HOT) are related to distortions of the electron distribution function from an isotropic Maxwellian that are even functions of $\mathbf{c}_e \equiv (\mathbf{v} - \mathbf{u}_e)$. Neglecting the HOT and evaluating the collisional term, $\frac{\delta q_e'}{\delta t}$, assuming all species other than the electron have Maxwellian distributions and neglecting terms of order m_e/m_i and m_e/m_n yields (18) [*Schunk and Nagy*, 2009]. In the collisionless limit, however, $\frac{\delta q_e'}{\delta t} \rightarrow 0$ by definition, and (53) ceases to give any information about the electron heat flux. In the collisionless limit the temperature gradient must be zero, or small if the HOT allow it, and the collisionless heat flow could be anything. Note the collisionless heat flow is a function of distribution function distortions from an isotropic Maxwellian that are odd functions of $\mathbf{c}_e$, and thus, it does not contribute to the HOT. The thermal electron equations used in the present model cannot account for these collisionless heat flows. Collisionless electron heat fluxes raise the high-altitude electron temperatures while still keeping the electron temperature profile nearly isothermal. Thus, collisionless heat fluxes would have similar effects to soft precipitation, which is not surprising. Distorting the "thermal" electron distribution to add a downward heat flow is equivalent to adding an additional "suprathermal" population of very soft precipitation.

As discussed above using (47), the FTICEHR is a useful albeit imperfect way to compare the effectiveness of suprathermal electrons to heat fluxes applied at the upper boundary. Reflected photoelectrons add a

FTICEHR in the range of 2–10 × 10^8 eV cm^{-2} s^{-1}, depending on the reflection potential and the solar conditions. The FTICEHR associated with polar rain is only 5–20% of the kinetic energy flux because higher-energy electrons are inefficient at heating the electrons. Nonetheless, for typical number fluxes of a few times 10^7 cm^{-2} s^{-1} the FTICEHR will be a few times 10^8 eV cm^{-2} s^{-1}. Thus, the FTICEHR associated with polar rain and reflected photoelectrons tend to be of comparable magnitudes. Polar rain, however, will create many more electrons through electron impact ionization than reflected photoelectrons. Dividing the heating between a larger population of electrons can reduce the observed electron temperature increase, or even produce an electron temperature decrease, with the addition of polar rain.

If temperature profiles extending well over 1000 km were available the effects of reflected photoelectron and thermal conduction could be distinguished. Simulations with reflected photoelectrons and zero thermal conduction become isothermal at the highest altitudes, but when thermal conduction is added the temperature profiles are constantly increasing. Typical macroscopic particle-in-cell (mac-PIC) simulations of the polar wind assume Boltzmannian electrons, which is only sensible if the electrons are isothermal [e.g., *Wilson et al.*, 1990; *Barakat et al.*, 1998a]. Few measurements of electron temperature profiles above 1000 km exist; these altitudes are challenging for incoherent scatter radars to reach given the low electron densities in the polar cap. *Kitamura et al.* [2011] presented electron temperatures from the Interkosmos mission extending to 3000 km. Although these measurements were compiled from multiple satellite passes and thus cannot be regarded as instantaneous temperature profiles, they are nonetheless fairly isothermal.

Kitamura et al. [2012] observed reflection potentials with a median of ~20 eV under solar maximum conditions, which is somewhat lower than the potentials estimated in the examples presented in this paper. The reflection potentials estimated by the automatic code which minimizes the electron velocity at the upper boundary depend on the ion outflow. If the model is underestimating the light ion outflow then it will overestimate the required reflection potential. The model neglects all ion kinetic physics above the ion exobase, temperature anisotropies, and centrifugal forces associated with convection, all of which could alter the amount of light ion outflow. However, because the differential energy flux of the photoelectron distribution peaks at ~20 eV, the FTICEHR of the reflected photoelectrons does not change much as the reflection potential is increased beyond 20 eV, as illustrated by Figure 3. Thus, even if the reflection potentials in this paper are overestimates, the associated FTICEHR are still reasonable.

Reflected photoelectrons cannot heat the nighttime ionosphere. The examples in this paper have focused on times near the summer solstice because during this time the flux tubes will be continuously sunlit as they convect around the polar cap. Figures 6 and 7 demonstrate that the plasma parameters change slowly with solar zenith angle as long as the Sun is up. Thus, for summer solstice simulations, the errors introduced by fixing the field line instead of following it around through a convection pattern are not very serious. In other seasons, however, the field lines can cross the terminator, possibly multiple times per day depending on the convection pattern. The plasma parameters are expected to be very different on the dayside and nightside of the terminator [*Kitamura et al.*, 2011; *Glocer et al.*, 2012], and every time a field line crosses the terminator in either direction it will exhibit transient behavior as it switches from one equilibrium to another. Nonetheless, RISR-N data from other seasons typically show the electron temperatures cooling down substantially at night. The temperatures do not go all the way down to the MSIS neutral temperatures, however. The small elevations in the nighttime electron temperatures could be explained by reasonable amounts of polar rain or could be residual heat from a time when the field line was on the dayside or in the auroral oval which has not dissipated in the time of convection to RISR-N's location. Either of these mechanisms could plausibly explain the nighttime RISR-N observations without needing to assume a significant amount of heat conduction down from the upper boundary.

6. Conclusions

This paper examines the effects of different kinds of energy flows into the polar ionosphere using a 1-D ionosphere-polar wind model developed for that purpose. The model allows energy to be input via thermal conduction, soft precipitation, and potentials which reflect photoelectrons. The examples presented confirm the findings of *Wilson et al.* [1997]; reflection potentials are required for sunlit polar cap field lines to achieve zero current without needing large amounts of cold electron inflow or heavy ion outflow. The model accounts for the extra heating from these reflected photoelectrons, and the flux tube integrated changes in the electron heating rates (FTICEHR) associated with reflected photoelectrons range from 2 to

10×10^8 eV cm^{-2} s^{-1}. Soft precipitation is shown to be rather inefficient at heating the thermal electrons because the cross sections for impact ionization of neutrals greatly exceed those for Coulomb collisions at energies of ~100 eV, but the associated FTICEHR can be comparable to those of reflected photoelectrons.

Simulations with reflected photoelectrons, zero FAC, and no other form of heat flux from the upper boundary can satisfactorily reproduce RISR-N plasma temperature measurements up to 600 km. Simulations with both reflected photoelectrons and polar rain can satisfactorily reproduce the measurements as well. Simulations with no reflected photoelectrons and downward FAC, however, systematically underestimate RISR-N temperature measurements. Reflected photoelectrons are a significant source of heat for the polar cap ionosphere which should be incorporated into future high-latitude ionosphere models. This goal will require a better understanding of the magnitudes and spatial distributions of the reflection potentials. In this paper the reflection potentials were set by simply assuming zero cold electron inflow or outflow at the upper boundary. The true physical processes governing the reflection potentials deserve further investigation.

Appendix A: Chemistry Model

In addition to all the ion-neutral reactions listed in Table 1 of *Richards* [2011], the model includes several additional light ion reactions which are summarized in Table A1. Furthermore, the density of N (^2D), the quenching of which is included as an electron heat source, is computed by assuming chemical equilibrium using the reactions in Table A2.

Table A1. Additional Ion Chemistry Added Beyond the *Richards* [2011] Model

Light Ion Chemistry		
Reaction	Rate (cm^3 s^{-1})	Reference
$H^+ + O \rightarrow O^+ + H$	$2.2 \times 10^{-11}\sqrt{T_{H^+}}$	*Schunk and Nagy* [2009]
$O^+ + H \rightarrow O^+ + O$	$2.5 \times 10^{-11}\sqrt{T_n}$	*Schunk and Nagy* [2009]
$He^+ + N_2 \rightarrow N_2^+ + He$	3.5×10^{-10}	*Huba et al.* [2000a]
$He^+ + N_2 \rightarrow N^+ + N + He$	8.5×10^{-10}	*Huba et al.* [2000a]
$He^+ + O_2 \rightarrow O_2^+ + He$	2.0×10^{-10}	*Huba et al.* [2000a]
$He^+ + O_2 \rightarrow O^+ + O + He$	8.0×10^{-10}	*Huba et al.* [2000a]
$H^+ + e \rightarrow H + h\nu$	$4.43 \times 10^{-12}\left(\frac{T_e}{300K}\right)^{-0.7}$	*Huba et al.* [2000a]
$He^+ + e \rightarrow He + h\nu$	$4.43 \times 10^{-12}\left(\frac{T_e}{300K}\right)^{-0.7}$	*Huba et al.* [2000a]
$O^+ + e \rightarrow O + h\nu$	$4.43 \times 10^{-12}\left(\frac{T_e}{300K}\right)^{-0.7}$	*Huba et al.* [2000a]
$N^+ + e \rightarrow N + h\nu$	$4.43 \times 10^{-12}\left(\frac{T_e}{300K}\right)^{-0.7}$	*Huba et al.* [2000a]

Table A2. Reactions Used to Compute Densities of N (^2D) in Chemical Equilibrium

N (^2D) Chemistry		
Reaction	Rate (cm^3 s^{-1})	Reference
$N_2^+ + O \rightarrow NO^+ + N(^2D)$	$1.33 \times 10^{-10}\left(\frac{T_i}{300K}\right)^{-0.44}$	*Richards* [2011]
$N_2^+ + e \rightarrow 2N(^2D)$	$2.2 \times 10^{-7}\left(\frac{T_e}{300K}\right)^{-0.39}$	*Richards* [2011]
$NO^+ + e \rightarrow O + N(^2D)$	$3.4 \times 10^{-7}\left(\frac{T_e}{300K}\right)^{-0.85}$	*Richards* [2011]
$N^+ + O_2 \rightarrow O_2^+ + N(^2D)$	$\begin{cases} 0.15 \times 5.5 \times 10^{-10}\left(\frac{T_i}{300K}\right)^{0.45} & T_i \le 1000\ K \\ 0.15 \times 9.5 \times 10^{-10} & T_i > 1000\ K \end{cases}$	*Richards* [2011]
$N(^2D) + e \rightarrow N(^4S) + e^*(+2.4\ eV)$	$6.5 \times 10^{-10}\sqrt{\frac{T_e}{300K}}$	*Aponte et al.* [1999]
$N(^2D) + O \rightarrow N(^4S) + O$	6.0×10^{-13}	*Aponte et al.* [1999]
$N(^2D) + O_2 \rightarrow NO + O$	6.0×10^{-12}	*Aponte et al.* [1999]
$N(^2D) + O_2^+ \rightarrow NO^+ + O$	1.8×10^{-10}	*Richards* [2011]
$N(^2D) + O_2^+ \rightarrow N^+ + O_2$	8.65×10^{-11}	*Richards* [2011]
$N(^2D) + O^+ \rightarrow N^+ + O$	1.3×10^{-10}	*Richards* [2011]

Appendix B: Derivation of the Ambipolar Electric Field

The thermal electron momentum equation is

$$\frac{\partial}{\partial t}\left(m_e n_e u_e\right) + \frac{1}{A}\frac{\partial}{\partial s}\left(A m_e n_e u_e^2\right) + \frac{\partial p_e}{\partial s} = -e n_e E_\parallel + \frac{\delta M_e'}{\delta t}, \tag{B1}$$

where $\frac{\delta M_e'}{\delta t} = \frac{\delta M_e}{\delta t} + m_e u_e \frac{\delta n_e}{\delta t}$. A suprathermal electron momentum equation is obtained by applying $2\pi m_e \int_{-1}^{1} \mathrm{d}\mu \int_0^\infty \mathrm{d}\mathcal{E}\, \mu$ to the time-dependent suprathermal electron transport equation (i.e., (13) plus $\frac{A}{v}\frac{\partial \Phi}{\partial t}$). The result is

$$\frac{\partial}{\partial t}\left(m_e n_s u_s\right) + \frac{1}{A}\frac{\partial}{\partial s}\left(A\mathcal{R}_s\right) + \frac{\partial \mathcal{P}_s}{\partial s} = -e n_s E_\parallel + \frac{\delta M_s'}{\delta t} \tag{B2}$$

where the relevant moments of the suprathermal electron spectrum are

$$\mathcal{P}_s \equiv 2\pi m_e \int_0^\infty \mathrm{d}\mathcal{E} \int_{-1}^{1} \mathrm{d}\mu \frac{1-\mu^2}{2}\mathcal{E}\Phi \tag{B3}$$

$$\mathcal{R}_s \equiv 2\pi m_e \int_0^\infty \mathrm{d}\mathcal{E} \int_{-1}^{1} \mathrm{d}\mu \frac{3\mu^2-1}{2}\mathcal{E}\Phi, \tag{B4}$$

and $\frac{\delta M_s'}{\delta t}$ is $2\pi m_e \int_{-1}^{1} \mathrm{d}\mu \int_0^\infty \mathrm{d}\mathcal{E}\, \mu$ applied to all the collisional terms.

Combining the thermal electron momentum equation, the suprathermal electron momentum equation, the ion momentum equations, and the definition of current density yields a generalized Ohm's law for the plasma.

$$\begin{aligned}\frac{m_e}{e}\frac{\partial J_\parallel}{\partial t} + \frac{1}{A}\frac{\partial}{\partial s}\left[A\left(\sum_i m_e n_i u_i^2 - m_e n_e u_e^2 - \mathcal{R}_s\right)\right] + \frac{\partial}{\partial s}\left(\sum_i \frac{m_e}{m_i} p_i - p_e - \mathcal{P}_s\right) \\ = \left(\sum_i \frac{m_e}{m_i} n_i + n_e + n_s\right) e E_\parallel + \sum_i \frac{m_e}{m_i}\frac{\delta M_i'}{\delta t} - \frac{\delta M_e'}{\delta t} - \frac{\delta M_s'}{\delta t}.\end{aligned} \tag{B5}$$

This Ohm's law is readily simplified with three approximations. First, neglect terms of order $\frac{m_e}{m_i}$. Second, assume the thermal electron and ion velocities are much less than the electron thermal speed, $\sqrt{\frac{k_B T_e}{m_e}} \approx 175$ km/s for a 2000 K plasma. This approximation means that the $m_e n_i u_i^2$ and $m_e n_e u_e^2$ terms are both negligible compared to p_e. Third, take the steady state limit and solve for the ambipolar electric field.

$$E_\parallel = \frac{-1}{e\left(n_e + n_s\right)}\left\{\frac{1}{A}\frac{\partial}{\partial s}\left(A\mathcal{R}_s\right) + \frac{\partial}{\partial s}\left(p_e + \mathcal{P}_s\right) - \frac{\delta M_e'}{\delta t} - \frac{\delta M_s'}{\delta t}\right\} \tag{B6}$$

This expression can be simplified even further by substituting the steady state limit of the suprathermal electron momentum equation:

$$E_\parallel = \frac{-1}{e n_e}\left\{\frac{\partial p_e}{\partial s} - \frac{\delta M_e'}{\delta t}\right\}. \tag{B7}$$

Expanding the electron collision terms results in

$$\begin{aligned}E_\parallel = \frac{-1}{e n_e}\Bigg\{\frac{\partial}{\partial s}p_e - m_e n_e \sum_i \nu_{ei}\left(u_i - u_e\right) - m_e n_e \sum_n \nu_{en}\left(u_n - u_e\right) \\ - \frac{m_e}{k_B T_e}\left(\frac{3}{5}\sum_i \nu_{ei} + \sum_n \nu_{en} z_{en}\right)\left(\frac{5}{2}\tilde{u}_e p_e - \kappa_e \frac{\partial T_e}{\partial s}\right) - C_{se} - m_e u_e \frac{\delta n_e}{\delta t}\Bigg\}.\end{aligned} \tag{B8}$$

The above equation uses the Burgers linear eight-moment collision term for electron-ion and electron-neutral interactions in the limit of small $\frac{m_e}{m_i}$ and small $\frac{m_e}{m_n}$ [*Schunk and Nagy*, 2009, equation

(5.127a)], and it uses (18) for the electron heat flow. The momentum transfer from suprathermal electrons to thermal electrons is

$$C_{se}(s) = 2\pi m_e \left\{ \int_{-1}^{1} d\mu \int_{0}^{\infty} d\mathcal{E} \frac{\mu}{m_e} \sqrt{\frac{m_e}{2\mathcal{E}}} L(\mathcal{E}) \Phi(s, \mathcal{E}, \mu) + \int_{-1}^{1} d\mu \int_{0}^{\infty} d\mathcal{E} \frac{3\mu^2 - 1}{2} D(\mathcal{E}) \Phi(s, \mathcal{E}, \mu) \right\}. \quad \text{(B9)}$$

Every term in (B8) goes to 0 as $m_e \rightarrow 0$ except the electron pressure gradient term. This explains why the eight-moment TRANSCAR model neglects these terms even though it includes all the other eight-moment collision terms [*Lilensten and Blelly*, 2002]. We have evaluated all these other terms with the real electron mass for the reference simulation and found that all except for one are at least 2 orders of magnitude smaller than the electron pressure gradient term, and thus can be omitted. The one extra term we will retain is the thermal conduction contribution to electron thermal diffusion. Even though m_e is small, κ_e is huge, so this term can be as much as ~50% of the thermal electron pressure gradient term. With this term included, the ambipolar electric field is

$$E_{\parallel} = \frac{-1}{en_e} \left\{ \frac{\partial}{\partial s} p_e + \frac{m_e}{k_B T_e} \left(\frac{3}{5} \sum_i \nu_{ei} + \sum_n \nu_{en} z_{en} \right) \kappa_e \frac{\partial T_e}{\partial s} \right\}, \quad \text{(B10)}$$

which is equivalent to (22). The models of *Schunk and Walker* [1969], *St.-Maurice and Schunk* [1977], and *Conrad and Schunk* [1979] are other examples of formulations where electron thermal diffusion is included alongside electron pressure gradients in expressions for the ambipolar electric field.

Acknowledgments

R.H. Varney is supported by the NASA Living With a Star Jack Eddy Postdoctoral Fellowship Program, administered by the University Corporation for Atmospheric Research. RISR-N was developed under the NSF cooperative agreement ATM-0121483 to SRI International, and the operations and maintenance are supported by NSF cooperative agreement ATM-0608577 to SRI International. The National Center for Atmospheric Research is sponsored by the National Science Foundation. The model source code, output data, and analysis routines used in this paper will be preserved on a long-term storage system. These items will be made available upon request to the authors. ISR data and analysis routines used in this paper are archived at SRI International and available upon request to the authors.

Michael Liemohn thanks Jean-Pierre St.-Maurice, Matthew Fillingim, and another reviewer for their assistance in evaluating this paper.

References

André, M., and A. Yau (1997), Theories and observations of ion energization and outflow in the high latitude magnetosphere, *Space Sci. Rev.*, *80*, 27–48.

Aponte, N., W. E. Swartz, and D. T. Farley (1999), Electron energy balance in the F region above Jicamarca, *J. Geophys. Res.*, *104*(A5), 10,041–10,049.

Axford, W. I. (1968), The polar wind and the terrestrial helium budget, *J. Geophys. Res.*, *73*, 6855–6859.

Bahcivan, H., R. Tsunoda, M. Nicolls, and C. Heinselman (2010), Initial ionospheric observations made by the new Resolute incoherent scatter radar and comparison to solar wind IMF, *Geophys. Res. Lett.*, *37*, L15103, doi:10.1029/2010GL043632.

Banks, P. M. (1966), Charged particle temperatures and electron thermal conductivity in the upper atmosphere, *Ann. Geophys.*, *22*, 577.

Banks, P. M., and T. E. Holzer (1968), The polar wind, *J. Geophys. Res.*, *73*, 6846–6854.

Banks, P. M., and T. E. Holzer (1969a), Features of plasma transport in the upper atmosphere, *J. Geophys. Res.*, *74*, 6304–6316.

Banks, P. M., and T. E. Holzer (1969b), High-latitude plasma transport: The polar wind, *J. Geophys. Res.*, *74*, 6317–6332.

Barakat, A. R., and R. W. Schunk (1984), Effect of hot electrons on the polar wind, *J. Geophys. Res.*, *89*, 9771–9783.

Barakat, A. R., H. Thiemann, and R. W. Schunk (1998a), Comparison of macroscopic particle-in-cell and semikinetic models of the polar wind, *J. Geophys. Res.*, *103*(A12), 29,277–29,287.

Barakat, A. R., H. G. Demars, and R. W. Schunk (1998b), Dynamic features of the polar wind in the presence of hot electrons, *J. Geophys. Res.*, *103*(A12), 29,289–29,303.

Bekerat, H. A., R. W. Schunk, and L. Scherliess (2007), Estimation of high-latitude topside electron heat flux using DMSP plasma density measurements, *J. Atmos. Sol. Terr. Phys.*, *69*, 1029–1048.

Blelly, P.-L., and R. W. Schunk (1993), A comparative study of the time-dependent standard, 8-, 13-, and sixteen-moment transport formulations of the polar wind, *Ann. Geophys.*, *11*, 443–469.

Burgers, J. M. (1969), *Flow Equations for Composite Gases*, Academic Press, New York.

Conrad, J. R., and R. W. Schunk (1979), Diffusion and heat flow equations with allowance for large temperature differences between interacting species, *J. Geophys. Res.*, *84*, 811–822.

Ganguli, S. B. (1996), The polar wind, *Rev. Geophys.*, *34*, 311–348.

Glocer, A., N. Kitamura, G. Toth, and T. Gombosi (2012), Modeling solar zenith angle effects on the polar wind, *J. Geophys. Res.*, *117*, A04318, doi:10.1029/2011JA017136.

Gombosi, T. I., and C. E. Rasmussen (1991), Transport of gyration-dominated space plasmas of thermal origin. 1. Generalized transport equations, *J. Geophys. Res.*, *96*(A5), 7759–7778.

Gustavsson, B., and B. Eliasson (2008), HF radio wave acceleration of ionospheric electrons: Analysis of HF-induced optical enhancements, *J. Geophys. Res.*, *113*, A08319, doi:10.1029/2007JA012913.

Hecht, J. H., T. Mulligan, J. T. Correira, J. H. Clemmons, D. J. Strickland, R. L. Walterscheid, and M. G. Conde (2012), A multiyear (2002–2006) climatology of O/N_2 in the lower thermosphere from TIMED GUVI and ground-based photometer observations, *J. Geophys. Res.*, *117*, A03302, doi:10.1029/2011JA017146.

Hoegy, W. R. (1984), Thermal electron heating rate: A derivation, *J. Geophys. Res.*, *89*(A2), 977–985.

Huba, J. D., G. Joyce, and J. A. Fedder (2000a), SAMI2 is another model of the ionosphere (SAMI2): A new low-latitude ionosphere model, *J. Geophys. Res.*, *105*(A10), 23035–23053.

Khazanov, G. V., T. Neubert, and G. D. Gefan (1994), A unified theory of ionosphere-plasmasphere transport of suprathermal electrons, *IEEE Trans. Plasma Sci.*, *22*(2), 187–198.

Khazanov, G. V., M. W. Liemohn, and T. E. Moore (1997), Photoelectron effects on the self-consistent potential in the collisionless polar wind, *J. Geophys. Res.*, *102*, 7509–7521.

Khazanov, G. V., M. W. Liemohn, E. N. Krivorutsky, and T. E. Moore (1998), Generalized kinetic description of a plasma in an arbitrary field-aligned potential energy structure, *J. Geophys. Res.*, *103*, 6871–6889.

Kitamura, N., Y. Ogawa, Y. Nishimura, N. Terada, T. Ono, A. Shinbori, A. Kumamoto, V. Truhlik, and J. Smilauer (2011), Solar zenith angle dependence of plasma density and temperature in the polar cap ionosphere and low-altitude magnetosphere during geomagnetically quiet periods at solar maximum, *J. Geophys. Res.*, *116*, A08227, doi:10.1029/2011JA016631.

Kitamura, N., K. Seki, Y. Nishimura, N. Terada, T. Ono, T. Hori, and R. J. Strangeway (2012), Photoelectron flows in the polar wind during geomagnetically quiet periods, *J. Geophys. Res.*, *117*, A07214, doi:10.1029/2011JA017459.

Kőrösmezey, Á., C. E. Rasmussen, and T. I. Gombosi (1993), Transport of gyration-dominated space plasmas of thermal origin. 2: Numerical solution, *J. Comp. Phys.*, *109*, 16–29.

Lemaire, J. F., W. K. Peterson, T. Chang, R. W. Schunk, A. R. Barakat, H. G. Demars, and G. V. Khazanov (2007), History of kinetic polar wind models and early observations, *J. Atmos. Sol. Terr. Phys.*, *69*, 1901–1935, doi:10.1016/j.jastp.2007.08.011.

LeVeque, R. J. (2002), *Finite Volume Methods for Hyperbolic Problems*, Cambridge Univ. Press, Cambridge, U. K.

Liemohn, M. W., G. V. Khazanov, T. E. Moore, and S. M. Guiter (1997), Self-consistent superthermal electron effects on plasmaspheric refilling, *J. Geophys. Res.*, *102*(A4), 7523–7536.

Lilensten, J., and P.-L. Blelly (2002), TEC and F2 parameters as tracers of the ionosphere and thermosphere, *J. Atmos. Sol. Terr. Phys.*, *64*, 775–793, doi:10.1016/S1364-6826(02)00079-2.

Mantas, G. P. (1975), Theory of photoelectron thermalization and transport in the ionosphere, *Planet. Space Sci.*, *23*, 337–354.

Moore, T. E., R. Lundin, D. Alcayde, A. Andre, S. B. Ganguli, M. Temerin, and A. W. Yau (1999), Source processes in the high-latitude ionosphere, *Space Sci. Rev.*, *88*, 7–84.

Palmadesso, P. J., S. B. Ganguli, and H. G. Mitchell (1988), Multimoment fluid simulations of transport processes in the auroral zones, in *Modeling Magnetospheric Plasma, Geophys. Monogr. Ser.*, vol. 44, edited by T. E. Moore and J. H. Waite, pp. 133–143, AGU, Washington, D. C.

Picone, J. M., A. E. Hedin, D. P. Drob, and A. C. Aikin (2002), NRLMSISE-00 empirical model of the atmosphere: Statistical comparisons and scientific issues, *J. Geophys. Res.*, *107*(A12), 1468, doi:10.1029/2002JA009430.

Prasad, S. S., D. J. Stickland, and Y. T. Chiu (1985), Precipitating electron interaction with the atmosphere. 2. The dayside cusp region, *J. Geophys. Res.*, *90*(A11), 11,025–11,034.

Richards, P. G. (2011), Reexamination of ionospheric photochemistry, *J. Geophys. Res.*, *116*, A08307, doi:10.1029/2011JA016613.

Richards, P. G., T. N. Woods, and W. K. Peterson (2006), HEUVAC: A new high resolution solar EUV proxy model, *Adv. Space Res.*, *37*, 315–322.

Schunk, R. W. (1975), Transport equations for aeronomy, *Planet. Space Sci.*, *23*, 437–485.

Schunk, R. W. (1977), Mathematical structure of transport equations for multispecies flows, *Rev. Geophys.*, *15*, 429–445.

Schunk, R. W. (2007), Time-dependent simulations of the global polar wind, *J. Atmos. Sol. Terr. Phys.*, *69*, 2028–2047, doi:10.1016/j.jastp.2007.08.009.

Schunk, R. W., and A. F. Nagy (2009), *Ionospheres: Physics, Plasma Physics, and Chemistry*, Cambridge Univ. Press, New York.

Schunk, R. W., and J. C. G. Walker (1969), Thermal diffusion in the topside ionosphere for mixtures which include multiply-charged ions, *Planet. Space Sci.*, *17*, 853–868.

Spitzer, L., Jr., and R. Härm (1953), Transport phenomena in a completely ionized gas, *Phys. Rev.*, *89*(5), 977.

St.-Maurice, J.-P., and R. W. Schunk (1977), Diffusion and heat flow equations for the mid-latitude topside ionosphere, *Planet. Space Sci.*, *25*, 907–920.

Su, Y., J. L. Horwitz, G. R. Wilson, P. G. Richards, D. G. Brown, and C. W. Ho (1998), Self-consistent simulation of the photoelectron-driven polar wind from 120 km to 9 R_E altitude, *J. Geophys. Res.*, *103*(A2), 2279–2296.

Tam, S. W. Y., F. Yasseen, T. Chang, and S. B. Ganguli (1995), Self-consistent kinetic photoelectron effects on the polar wind, *Geophys. Res. Lett.*, *22*, 2107–2110.

Tam, S. W. Y., F. Yasseen, and T. Chang (1998), Further development in theory/data closure of the photoelectron-driven polar wind day-night transition of the outflow, *Ann. Geophys.*, *16*, 948–968.

Tam, S. W. Y., T. Chang, and V. Pierrard (2007), Kinetic modeling of the polar wind, *J. Atmos. Sol. Terr. Phys.*, *69*, 1984–2027, doi:10.1016/j.jastp.2007.08.006.

Varney, R. H. (2012), Photoelectron transport and energy balance in the low-latitude ionosphere, PhD thesis, Cornell Univ., Ithaca, N. Y. [Available at http://ecommons.library.cornell.edu/bitstream/1813/31231/1/rhv5.pdf.]

Varney, R. H., W. E. Swartz, D. L. Hysell, and J. D. Huba (2012), SAMI2-PE: A model of the ionosphere including multistream interhemispheric photoelectron transport, *J. Geophys. Res.*, *117*, A06322, doi:10.1029/2011JA017280.

Wilson, G. R., C. W. Ho, J. L. Horwitz, N. Singh, and T. E. Moore (1990), A new kinetic model for time-dependent polar plasma outflow: Initial results, *Geophys. Res. Lett.*, *17*, 263–266.

Wilson, G. R., G. V. Khazanov, and J. L. Horwitz (1997), Achieving zero current for polar wind outflow on open flux tubes subjected to large photoelectron fluxes, *Geophys. Res. Lett.*, *24*, 1183–1186.

Yau, A. W., and M. André (1997), Sources of ion outflow in the high latitude ionosphere, *Space Sci. Rev.*, *80*, 1–25.

Yau, A. W., B. A. Whalen, T. Abe, T. Mukai, K. I. Oyama, and T. Chang (1995), Akebono observations of electron temperature anisotropy in the polar wind, *J. Geophys. Res.*, *100*, 17,451–17,463.

Yau, A. W., W. K. Peterson, and T. Abe (2011), Influences of the ionosphere, thermosphere and magnetosphere on ion outflows, in *The Dynamic Magnetosphere, IAGA Special Sopron Book Ser.*, vol. 3, edited by A. W. Yau, W. K. Peterson, and T. Abe, pp. 283–314, Springer, Dordrecht, Netherlands, doi:10.1007/978-94-007-0501-2_16.